Particuology 101 (2025) 18–32

Contents lists available at ScienceDirect

Particuology

journal homepage: www.elsevier.com/locate/partic

Review

Magnetic resonance imaging in granular flows: An overview of recent advances

Daniel A. Clarke [a], Willian Hogendoorn [b,*], Alexander Penn [c], Maria Raquel Serial [c]

[a] School of Chemical and Physical Sciences, Victoria University of Wellington, PO Box 600, Wellington, 6140, New Zealand
[b] Department of Process and Energy, Delft University of Technology, Leeghwaterstraat 39, 2628 CB, Delft, Netherlands
[c] Institute of Process Imaging, Hamburg University of Technology, Denickestraße 17, 21073, Hamburg, Germany

ARTICLE INFO

Article history:
Received 29 June 2023
Accepted 15 August 2023
Available online 1 September 2023

Keywords:
Magnetic resonance imaging
Granular flow
Multiphase flow
Recent advances in MRI

ABSTRACT

In this review we explore the recent developments in the use of Magnetic Resonance Imaging (MRI) for studying granular flows. While MRI has been a valuable tool in this field for the past 40 years, recent advances in imaging hardware, reconstruction software and particles synthesis have significantly enhanced its capabilities. This article provides an overview of the current challenges of MRI and progress in the field of granular media, and gives a perspective of the possible future developments in the field.

1. Introduction

Granular materials are widely encountered in natural and industrial contexts. Despite being widespread, we do not fully understand the material and flowing properties of granular systems. A key reason for this knowledge gap is the diversity of states in which these systems exist. Granular materials can exist in solid-like states such as soils, fluid-like states such as emptying through a silo and gas-like states such as pyroclastic flows. All these macroscale characteristics are governed by the interactions between individual grains that constitute the bulk material. The nature of the interactions between grains varies according to the size distribution, shape, and composition of the grains as well as the presence of interstitial fluid.

Building an understanding of granular materials requires detailed measurements of location, orientation, motion, and forces experienced by grains. Imaging is a useful method because it allows for information associated with many particles to be collected simultaneously. Optical imaging is limited to pseudo-2D systems because of the opacity of granular packings, even when individual grains are transparent. Thus, noninvasive imaging technology is required for acquiring detailed measurements of 3D granular systems.

Magnetic Resonance Imaging (MRI) is a noninvasive, 3D imaging modality that has been used for studying granular systems for the past 40 years. MRI is unique in being able to encode images with information about the velocity distribution, temperature and chemical composition. For this reason, it continues to be an important imaging tool to complement radiation-based methods that offer higher resolution and larger fields of view. Several reviews of MRI experiments on granular materials have been written during this period (Bonn et al., 2008; Fukushima, 1999; Kawaguchi, 2010), the most recent of which — to the authors' knowledge — was performed by Stannarius (2017). In addition to imaging of granular flows, MRI has been implemented extensively across various research fields, such as fluid mechanics and rheology (Coussot, 2020; Elkins & Alley, 2007), cardiovascular flows (Soulat, McCarthy, & Markl, 2020), and imaging in multiphase and granular materials (Gladden & Sederman, 2013). There have been many recent exciting developments in this area that demonstrate the usefulness of MRI as a tool for validating granular flow models and studying multiphase flows. Furthermore, progress in imaging hardware, reconstruction software, and experimental protocols has improved the MRI technique in the areas of time-resolved imaging and quantitative measurements. This review provides a brief summary of recent advances in MRI of granular flows since the mid-2010s to the present day. In particular, this review focuses on different studies and applications as compared to the scientific problems discussed in the review provided by Stannarius (2017).

* Corresponding author.
E-mail address: w.j.hogendoorn@tudelft.nl (W. Hogendoorn).

https://doi.org/10.1016/j.partic.2023.08.007

Additionally, perspectives on the future of the field is provided, outlining potential new lines of inquiry.

2. Fundamentals of MRI

2.1. Overview of NMR and MRI

The detailed fundamentals of MRI are well described in various textbooks (Callaghan, 1993; Brown, Cheng, Haacke, Thompson, & Venkatesan, 2014), where the latter also provides an overview of MR pulse sequence design. In the following a concise overview of the fundamentals underlying MR-based imaging is provided.

Several types of MRI system have been developed over the past decades. These MRI systems span from small benchtop configurations to human-scale clinical scanners. As each of these systems has its strengths and weaknesses, a summary of the performance of each category is provided in Table 1. A diagram of the main system components is shown by Fig. 1. All systems have these basic components in common (Webb, 2016):

(1) **Main magnetic field** (B_0) to polarise the sample. High-field systems ($B_0 > 1$ T) make use of helium-cooled superconducting electromagnets. The configurations vary from dipolar arranged systems to closed bore or cylindrical systems. Low-field systems typically comprise of an array of permanent magnets. For these systems the configurations vary from horseshoe or C-shaped magnets to Halbach arrays. Additional actively driven shim coil electromagnets (resistive shims), and/or pieces of soft iron mounted on the inner surface of the magnet (passive shims) are used to increase the homogeneity of the main magnetic field — and thus improve measurement accuracy.

(2) **Gradient coils.** These coils generate a magnetic field in addition to the main field that varies linearly across the imaging region. These coils enable the spatial encoding of the MR signal. There are usually three coils, one for each Cartesian coordinate axis relative to the direction of the main field. The coils generally require significant current amplification and cooling to produce gradients strong enough for imaging purposes.

(3) **RF transmit and receive coils.** Transmit coils produce a magnetic field (B_1) orthogonal to the static field that excites the sample to produce a signal, while receive coils detect this signal. Systems may comprise of a single transmit/receive RF coil such as used in microimaging systems, to RF coil arrays used for parallel imaging in clinical systems. Nowadays typically quadrature (or circularly polarized) coils are used, as they provide $\sqrt{2}$ more signal compared to linear receiver coils.

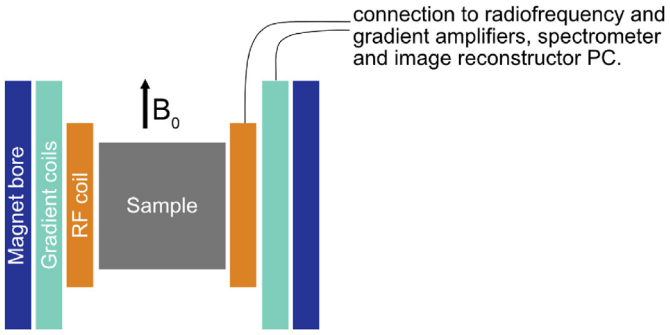

Fig. 1. Schematic of the main components in the usual MRI setup: magnetic field B_0, gradient coils, and RF transmit/receive coil.

MRI, also known as nuclear magnetic resonance (NMR) imaging, makes use of the nonzero net magnetic moment of nuclei. Common naturally present isotopes used in MRI include ^{1}H (also referred to as proton imaging), ^{13}C, ^{23}Na, ^{27}Al, ^{31}P, and ^{129}Xe. When exposed to a main magnetic field, B_0, the unpaired nuclear spins of these isotopes interact with this external field, resulting in a net magnetisation (M_0) within the sample. The characteristic time-scale related to this (re-)magnetisation is the so-called spin-lattice or longitudinal relaxation time, T_1. Note that T_1 is sample-specific and therefore can be used as a means of contrast to distinguish between different materials.

An MR signal is created by a radiofrequency (RF) pulse, tuned to the Larmor frequency of the sample in the static magnetic field B_0. This results in a transverse magnetisation component, with an associated timescale T_2. This transverse magnetisation is detected by the receiver coils and is known as the free induction decay (FID), shown in Fig. 2(a). The FID is a combination of all of the induced voltages from the precessing magnetisation elements in the sample. If there are elements of the magnetisation precessing at different frequencies, these can be decomposed into a power spectrum via discrete Fourier transform. The spectral peaks act as unique identifiers for nuclei in distinct electronic environments, where the amplitude is related to the relative amount of nuclei belonging to a functional group. This spectral sensitivity means that

Table 1
Typical specifications for different MRI systems.

	Benchtop	Microimaging	Pre-clinical	Clinical
Common commercial vendors (whole systems)	Pure devices, Resonint	Bruker	Bruker, MR Solutions, Aspect Imaging	Siemens, Philips, GE Healthcare, Toshiba, United Imaging, Canon Medical, Aspect Imaging, Hyperfine
Approx. cost (USD)	10^4	10^6	10^6	$\geq 2 \times 10^6$
System footprint[a] (m^2)	0.3	15	25	50
Field (T)	0.3–0.5	7.0–18.8	1.0–15.2	1.0–14
Bore orientation	Vertical	Vertical	Horizontal and Vertical	Horizontal
Max. sample diameter (m)	0.015	0.03	0.07–0.18	0.7
Typical voxel size (μm)	100	50	150	1000
Max. gradient (T m^{-1})	0.15	1.5	1.0	0.200
Helium loss rate (mL h^{-1})	Nil	13	Nil[b]	Nil[b]
Max. slew rate (T m^{-1} s^{-1})	1500	10000	9000	250
Ref.	(Pure Devices GmbH, 2019; Resonint Ltd, 2022)	(Bruker Corporation, 2023)	(Bruker Biospin, 2020; MR Solutions Group Ltd., 2020)	(Zenger, 2014; Hyperfine, Inc., 2023)

[a] Considering magnet, console, and other required infrastructure.
[b] In case of zero boil-off technique for systems that use cryogens.

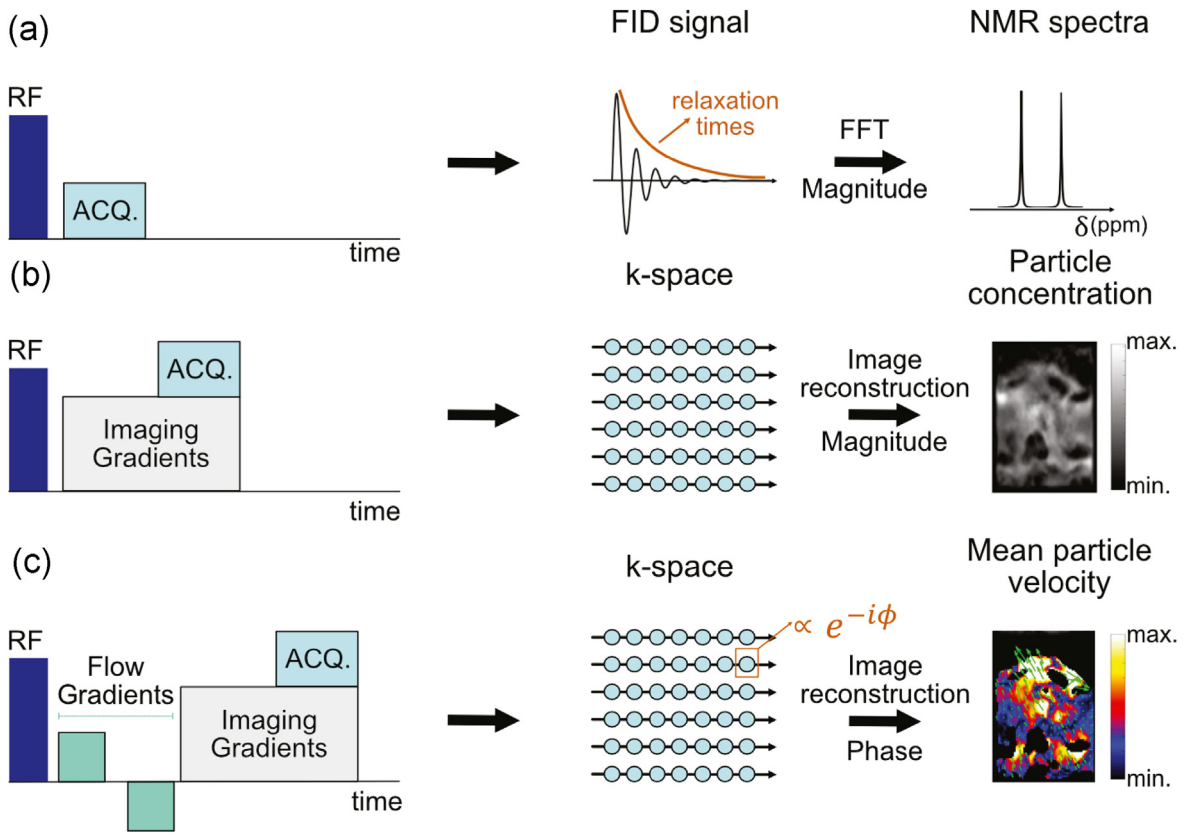

Fig. 2. Schematic representations of (a) a typical NMR excitation pulse sequence, including FID detection and associated NMR spectra, (b) MRI pulse sequence for particle concentration imaging, including acquired 2D *k*-space and the obtained magnitude image, and (c) MRI pulse sequence for velocity mapping, including obtained velocity maps. Particle concentration and mean velocity maps are adapted with permission from Penn et al. (2018). Copyright 2018 American Chemical Society.

it is possible to run spectrally selective experiments that isolate a particular material by carefully selecting the nucleus that is studied.

The frequency of the magnetisation, also known as Larmor frequency, is proportional to the applied magnetic field. Therefore, spatial localisation can be achieved by adding spatially and temporally varying magnetic fields to the static magnetic field. These so called magnetic field imaging gradients are produced by gradient coils (Fig. 1) and span the imaging *k*-space as shown by Fig. 2(b). As a result, the FID turns into a combination of different precession frequencies that depend on the spatially-varying local magnetic field. When performing an MRI experiment, signal is usually sampled and stored in *k*-space, a mathematical space representing spatial frequencies in an MRI image. Fourier transform of the *k*-space returns the spectral density of the sample — which depends on the spin density and signal decay caused by relaxation — at a given position in space. This spatial domain spectrum is what is referred to as the image.

2.2. Information obtained with MRI

Due to the unique way NMR data is collected, an image is an array of complex numbers, each voxel has a magnitude and phase angle. This wealth of information is used to obtain measurements of different variables pertinent to granular flows.

2.2.1. Particle volume fraction

Because image intensity scales linearly with spin density, the particle volume fraction is found from the magnitude of the image as shown by Fig. 2(b). To ensure that the measurement is quantitative, a B_1 map is needed to account for variations in the B_1 field that may be mistaken for packing variations. A calibration curve is required to convert the arbitrary units of the image intensity to volume fraction units. The best results are obtained with an internal reference that can be used to correct for field drift and tuning variations (Mehdizad, Fullard, Galvosas, & Holland, 2021).

2.2.2. Mean velocity

Nowadays, the most often used method for average velocity acquisition is the phase-contrast (PC) method illustrated in Fig. 2(c). Time-of-flight and spin labelling (or tagging) methods are rarely used outside specific medical applications owing to lower resolution and lower accuracy compared to PC MRI (Moser et al., 2000). In PC MRI, contrast in the phase of the image is used to determine the local mean velocity of the flow. The magnetisation is dephased by a gradient pulse, the flow is left to evolve during an observation delay, followed by an opposite gradient pulse that rephases the magnetisation. For nuclei that have displaced during the delay, the dephasing and rephasing effects do not cancel out and a net phase shift proportional to the mean displacement of nuclei located within the image voxel remains (Gladden & Sederman, 2013).

2.2.3. Velocity fluctuations

The pulse sequence used in phase contrast velocimetry is identical to diffusion NMR, which operates on the principle that phase dispersion caused by diffusing molecules attenuates the NMR signal. In granular materials, the velocity fluctuations of individual grains relative to the mean flow produces a similar effect. The variance of velocity is determined from the signal attenuation. Interpreting velocity variance is challenging because it depends on

the observation delay used (Holland, Müller, Dennis, Gladden, & Sederman, 2008). It is common to assume that the velocity fluctuations follow a Gaussian distribution. While this assumption holds well for rapid granular flow, significant errors can be generated if the distribution of velocity fluctuations is not described correctly (Schmidt et al., 2021). Therefore, *a priori* flow information is required to reliably apply this measurement method. For cardiovascular flow applications a multipoint phase-contrast method in combination with a Bayesian analysis provides consistently lower errors (Binter, Knobloch, Manka, Sigfridsson, & Kozerke, 2013; Dirix, Buoso, Peper, & Kozerke, 2022). Velocity gradients below the scale of the voxel size also contribute to phase dispersion and may require a different model for signal attenuation (Dyverfeldt, Sigfridsson, Kvitting, & Ebbers, 2006). Furthermore, rotational motion of the granules may also affect the signal attenuation and amplify the measured velocity variance (Clarke, Fabich, Brox, Galvosas, & Holland, 2019). Variations in the mean flow during the experiment, referred to as the "bubble-like" granular temperature (Jung, Gidaspow, & Gamwo, 2005), also contribute to the velocity variance (Müller et al., 2008). For these reasons, MRI does not measure the true "particle-like" granular temperature. Nonetheless, the velocity variance measurements provide deep insights into spatial and temporal fluctuations in granular systems.

2.2.4. Spectral imaging

NMR spectra can be obtained with spatial localisation using imaging methods such as single voxel imaging or chemical shift imaging (CSI). In these instances, spatial localisation is performed, followed by recording the FID. For CSI, each voxel has an associated NMR spectrum, which is used to elucidate information about chemical composition and temperature. Chemical composition maps can be generated for reacting systems by integrating the relevant peaks in the measured spectra (Ulpts, Dreher, Klink, & Thöming, 2015). The main disadvantage with CSI is that *k*-space data is acquired one point at a time, which leads to long experiment times and low image resolution. However, *a priori* knowledge of the spectral characteristics can be used to develop reconstruction algorithms to obtain composition maps from rapidly acquired image data (von Harbou et al., 2015).

2.2.5. Temperature imaging

The aforementioned MRI-based measurement modalities can be extended with MR Thermography (also referred to as Thermometry), which allows for the measurement of three-dimensional temperature fields. All existing methods make use of an indirect measurement approach, where the temperature is inferred from properties of the sample that can be measured by the MRI system. These properties include relaxation times contrast, molecular self-diffusion coefficient, or the resonance frequency of a specific chemical species (Webb, 2002). Spectroscopic imaging is also useful for temperature measurements because nuclei in particular chemical environments have temperature-dependent chemical shift relative to a reference peak, e.g., ethylene glycol (Gladden et al., 2010). Among the various thermometry techniques, the proton resonance frequency (PRF) shift method is the most widely used method in medical diagnosis interventions, such as high-intensity focused ultra-sound (HIFU), radiofrequency (RF) hyperthermia and RF ablation. The PRF method makes use of the fact that the chemical shift for ^{1}H nuclei involved in hydrogen bonding varies linearly with temperature (Hindman, 1966). Therefore, the local magnetic field deviation is proportional to the local temperature. If the proton resonant frequency is calibrated against the known temperature, then a magnetic field map can be converted into a temperature map (Bruschewski, Schmidt, John, Grundmann, & Schmitter, 2021; Serial et al., 2023; Wlodarczyk et al., 1999).

2.3. Current challenges for MRI and granular systems

The considerably short-lived signals observed in typical granular systems often limit the direct applicability of MRI techniques. In this sense, it is important to consider both the NMR properties of the granular particles and the MRI pulse sequence used, as they play crucial roles in determining the quality of the resulting image.

While plant seeds are widely used to investigate dry granular flow due to their high oil content, they typically give low signal amplitude, and their complex chemical composition introduces magnetic field inhomogeneities that rapidly decay the signal. The time constant of this decay is much smaller than the intrinsic T_2 relaxation, and is denoted as T_2^*. This limits the available time to encode the image and capture flow details. To overcome these limitations, porous particles soaked in liquid (Holland, Müller, Dennis, Gladden, & Davidson, 2010) or liquid-filled core-shell particles (Penn et al., 2017) have been investigated as possible alternatives. Engineered materials have the advantage of a higher liquid content, resulting in increased signal-to-noise ratio (SNR) and a reduction in local field inhomogeneity. Moreover, the composition of the liquid solution in the capsules can be adjusted to be temperature-sensitive (Gladden et al., 2010), or matched in susceptibility to the interstitial fluid (Serial et al., 2023). See Table 2 for a selection of commonly used granular particles, including the corresponding T_2 and T_2^* time constants.

The NMR signal of granular media is also influenced by magnetic susceptibility mismatch between the particles and interstitial fluid. As a result, pulse sequences that are robust to magnetic field inhomogeneities, such as spin echo based sequences, are commonly preferred. Alternatively, ultra-short echo time (UTE) pulse sequences can be used, where the frequency encoding begins shortly after RF excitation reducing the scan time to as short as 1 ms (Fabich, Sederman, & Holland, 2016).

To mitigate the impact of short-lived signals in granular media, various acceleration techniques can be employed to shorten image acquisition. These techniques typically involve one or a combination of single-shot readouts, parallel imaging (Griswold et al., 2002; Pruessmann, Weiger, Scheidegger, & Boesiger, 1999; Sodickson & Manning, 1997), multi-band acquisition imaging, such as Simultaneous Multi-Slice (SMS) (Müller, 1988) or CAIPIRINHA approaches (Blaimer, Choli, Jakob, Griswold, & Breuer, 2013; Breuer et al., 2005) and compressed sensing reconstruction (Candes, Romberg, & Tao, 2006; Lustig, Donoho, & Pauly, 2007) among others. Table 3 lists commonly used acceleration techniques along with their corresponding acceleration factor *R* defined as the ratio of the portion of the image acquired in a fully sampled manner to the amount acquired in the accelerated acquisition.

3. Current use of MRI in granular and multiphase systems

MRI has been successfully applied to a range of granular and multiphase systems. In particular, MRI provides valuable insight in process conditions, as it unveils the 3D flow dynamics of (downscaled) industrial applications. These applications are highly case-specific due to the unique particle material properties. In this section recent studies are highlighted, summarizing the potential of MRI.

3.1. Rheo-NMR

Continuum modelling of granular flow requires a constitutive equation for the stress tensor to close the volume-averaged Navier-stokes equations (Anderson & Jackson, 1967). Rheo-NMR integrates NMR technology with rheology to aid in the characterisation of

Table 2
A selection of commonly used granular particles.

Particle	Average d [mm]	Typical T_2 [ms]	Typical T_2^* [ms]	Ref.
Poppy seeds	1.3	75	1.4[a]	(Penn et al., 2017; Fullard et al., 2019; Boyce et al., 2016)
Iceland poppy seeds	0.5–0.7	–	–	(Müller et al., 2006; Köhl et al., 2013)
Mustard seeds	1.3–1.7	25–50	1.5[a]	(Mehdizad et al., 2021; Penn et al., 2017; de Cagny, Fall, Denn, & Bonn, 2015; Fabich, Sederman, & Holland, 2017; Fabich et al., 2018; Boyce, Penn, Pruessmann, & Müller, 2018; Boyce, Penn, Lehnert, Pruessmann, & Müller, 2019a)
Lobelia seeds	0.44	25–50	0.1	(Fabich et al., 2017; Fabich et al., 2018)
Nicotiana seeds	0.72	25–50	0.1	(Fabich et al., 2016, 2017)
Petunia seeds	0.63	25	0.1	(Fabich et al., 2018)
Agar shell particles filled with MCT oil	1.02 ± 0.12	–	1.8	(Penn et al., 2017, 2019; Penn, Boyce, Pruessmann, & Müller, 2020; Boyce et al., 2019; Boyce et al., 2019b)
Silica-alumina particles soaked in doped water	~ 0.06	3	–	(Holland et al., 2010)
Phase change material (PCM) particles	3.5	–	–	(Skuntz, Perera, Maneval, Seymour, & Anderson, 2018, 2021)
Polypropylene particles filled with aqueous solution	10	–	–	(Serial et al., 2023)
Hydrogel particles	2.5–7.0	–	–	(Wang et al., 2022)

– Refers to not available data.
[a] Penn et al. (2017).

Table 3
Scan time acceleration techniques, their main drawbacks, and corresponding acceleration factors (R). Depending on the application, different techniques can be combined to further increase R. Listed specifications are taken from Kozak, Jaimes, Kirsch, and Gee (2020).

Technique	Description	Main drawbacks	Typical R
Parallel imaging	A reduced portion of the image is simultaneously acquired by an array of receiver coils	Decreased SNR, residual aliasing	1.5–4.0
Compressed Sensing	Exploits the underlying structure in images to reconstruct them using undersampled data	Limited applicability to sparse signals, long reconstruction times	2.0–15.0
Simultaneous Multi-Slice	Simultaneous excitation of multiple slices by means of multi-band RF pulses and multi-rf receiver coil acquisition	Residual aliasing	2.0–8.0

complex fluids (Callaghan, 1999). Rheo-NMR measures local velocity within a sample, producing detailed local shear data. Furthermore, spectroscopic data provides information about the composition of the fluid. Rheo-NMR can also be applied to granular systems in order to gain useful insights towards developing accurate models for granular rheology. The annular Couette shear cell is the most widely used geometry which is comprised of a rotating inner cylinder centred inside a hollow outer cylinder, with the sample material filling the gap. Rheo-NMR experiments are typically carried out using a commercially available Rheo-NMR hardware produced by Magritek Ltd. and distributed by Bruker Biospin GmbH, specifically designed for wide-bore superconducting magnet devices (see Fig. 3). However, custom-built geometries and drive systems can also be found in literature (Brox, 2016; Milc et al., 2022; Serial, 2018; Serial et al., 2019), including studies conducted in medical scanners (Ovarlez et al., 2008; Wang et al., 2022).

Rheo-NMR has been used to study granular systems for the last 25 years (Mueth et al., 2000). During this time, there have been developments in the application of the NMR technique, rheo-NMR drive systems (Brox, 2016), and in granular rheology modelling. Local rheology models such as the viscoplastic $\mu(I)$ model (Jop, Forterre, & Pouliquen, 2006) do not accurately describe granular flow in a Couette cell because of the nonuniform stress state that exists across the gap (Koval, Roux, Corfdir, & Chevoir, 2009). For this reason, nonlocal rheology models have been the subject of testing using rheo-NMR. Volume fraction and velocity measurements show that the nonlocal fluidity model accurately describes the velocity across the gap for dense particle suspensions. Nonlocality was related to the gradient in the volume fraction induced by the nonuniform shear stress across the gap (de Cagny et al., 2015). Velocity variance data were used to assess the shear rate-granular

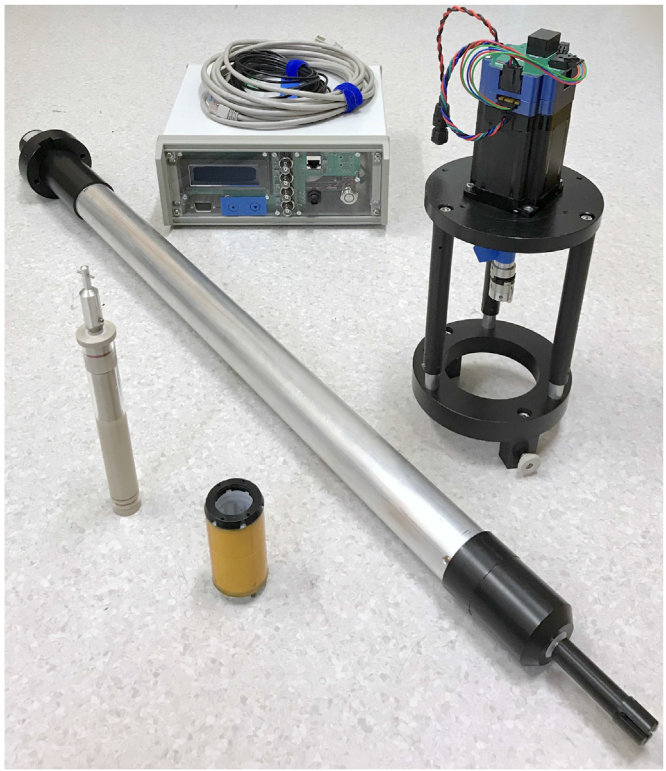

Fig. 3. Components of Magritek Rheo-NMR kit such as controller module (top center), motor, gearbox, and mounting unit (top right), drive-shaft (diagonal), shear device (left), and RF coil (lower left). Reproduced with permission from Stevenson (2018).

temperature scaling relations predicted by fluidity and kinetic theory models (Fabich et al., 2018). These data indicated that the fluidity model scaling exponent was not valid, while the kinetic theory scaling exponent was consistent with optical measurements of the free surface (Bocquet, Losert, Schalk, Lubensky, & Gollub, 2001).

3.2. Hoppers

A hopper is a vessel widely used in agriculture and industry to store and disperse granular materials. Hopper flow characteristics are highly variable depending on the granular material properties and the hopper geometry. From an operational perspective, poorly optimised hopper geometry can result in blockages and inadequate blend quality for mixtures. MRI has been used to visualise flow in 3D hoppers and providing data against which models can be validated.

MRI experiments have been performed using microimaging systems for small hoppers (diameter $\approx$ 30 mm) using plant seeds as the signal source. Volume fraction measurements inside a hopper were first obtained by Gentzler and Tardos (2009) using the single point imaging (SPI) imaging sequence (Balcom, 1996; Emid & Creyghton, 1985). These measurements were normalized against the volume fraction of a static system. The image intensity is in arbitrary units, thus it is necessary to calibrate the signal intensity for known volume fractions in order to obtain volume fraction images. This approach was used to attain volume fraction measurements with a quantitative accuracy within 2% (Mehdizad et al., 2021). In these cases, SPI techniques were used because the scan time was sufficiently short that any motion artefacts had minimal influence on the measured image intensity.

SPI volume fraction and spin-echo velocity measurements can be used to attain insights into the characteristics of granular flow in hoppers. For example, the phenomenon of self-similar volume fraction and velocity profiles across the hopper outlet was found to hold for 3D systems (Mehdizad et al., 2021). The velocity gradient was found to vary smoothly along the height of the hopper, which suggests that the “free fall arch” model (Brown & Richards, 1965) for discharge through a hopper is not valid. In addition, measurements were performed using inserts inside the hopper. Solid volume fraction variations near the insert and velocity data were used to analyse modified flow patterns that could increase the discharge rate and remove static zones (Mehdizad, 2021). Experiments involving non-spherical particles were also performed, which illustrated that particle shape played an important role in the flow field characteristics.

The unsuitability of macroscale models for describing flow through hoppers necessitates the use of more detailed models to accurately capture the flow dynamics. To this end, MRI velocimetry experiments of hopper flow were compared to discrete element modelling simulations of equivalent geometry (Danczyk et al., 2020). It was found that the simulations gave the best quantitative agreement with experiments when the contact parameters were set to empirically determined values, lending confidence to the validity of the assumptions used to develop the discrete element method.

MRI velocimetry was also used to investigate the validity of continuum simulations, namely the volume-averaged Navier-Stokes equations using the $\mu(I)$ rheology to describe the stress tensor. The $\mu(I)$ model could qualitatively reproduce the velocity field, but not quantitatively match the overall flow rate exiting the hopper (Fullard et al., 2019). By varying the hopper angle and wall roughness, distinct flow regimes were observable. The $\mu(I)$ model could describe the mass flow and funnel flow regimes, but could not reproduce the “rat-holing” behavior observed for rough walls. A key limitation of this continuum model was that incompressible flow was assumed. In reality, the flow is compressible, as illustrated by the measured variations in the volume fraction. It is likely that compressibility will be a necessary addition to improve the predictive ability of continuum models.

3.3. Gas-solid fluidized beds dynamics

Gas-solid fluidized beds are commonly used in various industrial processes, including energy conversion, pharmaceuticals, and food production. These systems consist of a column filled with granular particles, typically less than 1 mm in size, through which gas is injected from the bottom. At sufficiently high velocities, drag force balances the gravitational force on the particles, resulting in “fluid-like” behavior. As the gas velocity increases, different fluidization regimes can occur, including bubbling, slugging and turbulent fluidization (Kunii & Levenspiel, 1991).

MRI represents a powerful tool to study the flow patterns of particles and gas (Boyce, Rice, Ozel, et al., 2016), and local particle concentrations within fluidized beds. Unlike other tomography methods such as X-ray tomography (Mudde, 2010), positron emission particle tracking (Wildman, Huntley, Hansen, Parker, & Allen, 2000) and electric capacitance tomography (Chandrasekera et al., 2015), MRI can provide 3D information about particle distribution, velocity, chemical composition, and temperature.

To accurately capture the complex nonstationary flow dynamics that occur within fluidized beds, the temporal resolution of the MRI sequence must be comparable to the characteristic timescale of the system. This timescale is in the range of several milliseconds for millimeter-sized particles. Therefore, recent efforts have focused on implementing real-time MRI techniques to successfully capture instantaneous particle dynamics. For instance, Fabich et al. have recently employed a UTE MRI approach combined with Compressed Sensing to capture the dynamics of a 3D gas-solid fluidized bed in less than 40 frames per second (Fabich et al., 2016, 2017). Fig. 4(a) shows a schematic of the employed experimental setup describing the glass column running through the microimaging MRI magnet. The short acquisition time, enabled to combine 1D and 2D images to simultaneously track and measure the bubble rise velocity and visualise in-plane bubble behavior shown by Fig. 4(b) and (c).

Another way to decrease image acquisition time is to combine MRI scan acceleration techniques and adapt them to the signal properties of the MRI-active granular material. Penn et al. (2017) demonstrated this approach on a clinical MRI system equipped with a custom-built 16-channel radio-frequency receiver array, running single-shot echo planar imaging (EPI) pulse sequences with Partial Fourier combined with an appropriate parallel imaging (SENSE) reconstruction algorithm. The readout duration of the pulse sequences were adapted to the effective transversal relaxation time (T_2^*) of the imaged granular material, namely engineered oil-filled agar capsules. The temporal and spatial resolution of the 2D image time series were 7 ms and 3 mm $\times$ 3 mm $\times$ 10 mm for the spin density measurements and 21 ms and 3 mm $\times$ 5 mm $\times$ 10 mm for the phase contrast, in-plane particle velocity measurements. (Penn et al., 2017). Fig. 5(a) illustrates the 16-channel receiver coil array surrounding the gas-solid system used, which was placed inside a medical MRI scanner for experiments as shown by Fig. 5(b). This method was used to investigate various hydrodynamic phenomena occurring in gas-solid systems, including (i) the gas bubble behavior and particle flow characteristics of dry (Penn et al., 2018) and wet (Boyce et al., 2018) freely bubbling fluidized beds (ii) the effect of internals within fluidized beds on the fluidization hydrodynamics (Buchholz, Brummerloh, Benders, & Penn, 2023; Penn

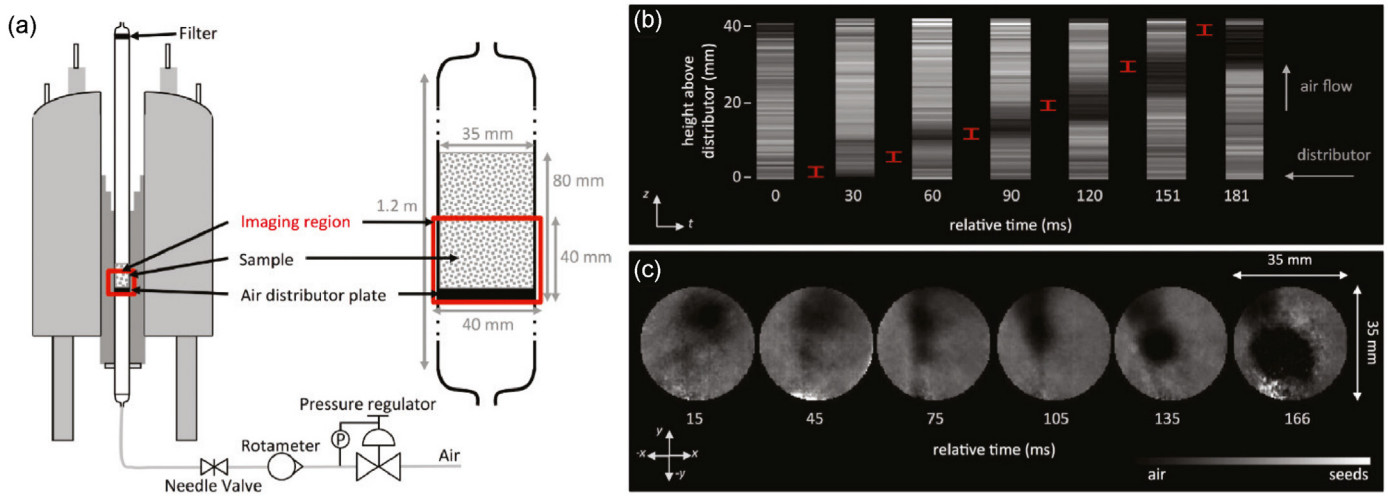

Fig. 4. (a) Schematic of the experimental apparatus employed by Fabich et al. (2017): a glass column runs through the center of the MRI magnet shown in grey. Gas flow is inserted from the bottom by means of a pressure regulator. The imaging region is highlighted in red, showing the bed dimensions. (b) 1D profiles along the z-axis and (c) 2D axial images of a fluidized bed of Nicotiana seeds.

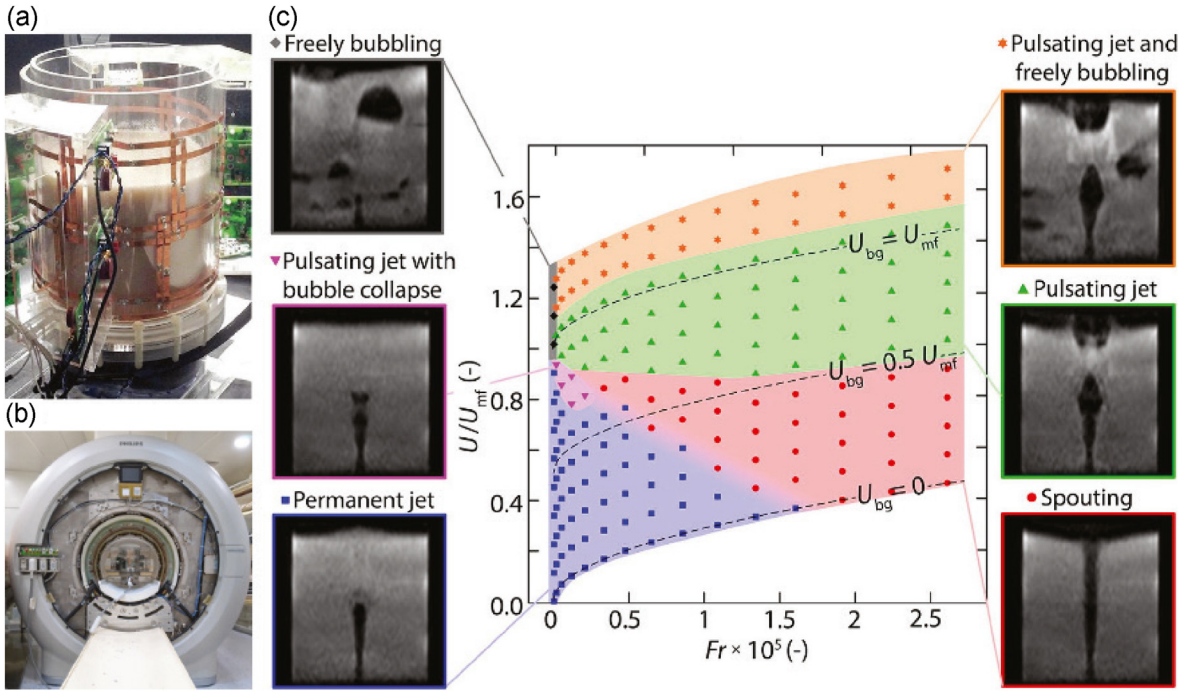

Fig. 5. Experimental setup employed by Penn et al. (2017) for real-time MRI experiments: (a) fluidized bed placed in the multi-array receiver coil and (b) medical scanner used for experiments with the fluidized bed setup inside. (c) A map showing the different regimes formed by injecting air through a central orifice into a fluidized bed (Penn et al., 2020).

et al., 2019), (iii) bubble dynamics during gas injection into fluidized beds (Boyce et al., 2019a; Boyce et al., 2019b; Boyce et al., 2019) and (iv) the anomalous sinking of intruders into aerated granular packings (Tsuji et al., 2021). More recently, Penn et al. (2020) employed this technique to identify and characterize the different flow regimes encountered during gas injection. Fig. 5(c) shows MRI images corresponding to the six identified flow regimes, plotted as a function of normalized jet velocity and the Froude number, defined as the ratio of the inertial forces to the gravitational forces acting on the particles (Penn et al., 2020). The measurement of instantaneous velocities of the particles allowed the establishment of an empirical model for predicting the jet length as a function of the background gas flow and gas flow injected through the orifice.

3.4. Particle-laden pipe flows

Also in the field of (dense) suspension flows the potential of MRI-based experiments was discovered. About one decade after the first successful NMR exam on a live human person, pioneering experiments were conducted on particle-laden flows by Majors, Givler, and Fukushima (1989). Since then, these particle-laden systems have been studied continuously using MRI (e.g., Altobelli, Givler, & Fukushima, 1991; Hampton, Mammoli, Graham, Tetlow, & Altobelli, 1997; Han, Kim, Kim, & Lee, 1999; Leskovec, Lundell, & Innings, 2020), because of their relevance for a range of applications including (domestic) slurry transport, 3D printing, and food processing. Despite these previous research efforts, many open

questions remain for suspension flows, for instance related to the development length of these systems, or the exact velocity and spatial particle distribution profiles. The latter are found to dictate the pressure drop required for the transport of these suspensions (Hogendoorn et al., 2023).

The strength of MR-based measurements is the simultaneous acquisition of 3D (time-averaged) velocity and concentration fields, even for densely-laden flows which are optical in-accessible. See e.g., Fig. 6 for a camera image of such a particle-laden flow. The liquid phase velocity, u_l, and solid volume fraction, φ_s, profiles representing the flow conditions in the mid-plane are superimposed on this image. The markers are results obtained using MRI and the solid lines are results from direct numerical simulations (DNS). MRI provides valuable quantitative information about the flow patterns and corresponding flow characteristics. Typically the fluid phase is used for the MR signal (proton imaging), whereas the magnetically transparent particles cause a reduction in this signal as they occupy space of the hydrogen protons. From a combination of the time-averaged solid volume fraction distribution and the velocity profile, the actual liquid velocity distribution can be determined (Hogendoorn et al., 2023). This is required since the particles are non-homogeneously distributed in the radial direction.

Until recently, MRI experiments were predominantly performed in the low Reynolds number (i.e., viscous) regime in order to avoid inertial effects. This legitimized the time-averaged velocity and concentration measurements so far. However, most industrial processes are dominated by inertial effects. For these applications, insight in turbulent and particle stresses is required for the modelling of these flows. In a recent study, Leskovec et al. (2020) presented velocity variance measurements in particle-laden flows. Their protocol is developed by MacKenzie, Söderberg, Swerin, and Lundell (2017) which is adapted from Elkins and Alley (2007) and Dyverfeldt et al. (2006). However, since the frequency of MRI acquisitions is bounded by the repetition rate, variance measurements in turbulent flows are limited to flows where the characteristic time scale of the energy containing turbulent eddies can be captured with the MRI protocol. Generally, the flow-encoding duration—and thus the sample frequency—of MR systems are considerably higher than the timescale of velocity fluctuations. Standard PC-MRI sequences cannot resolve motion on the characteristic time scale. However, modulated gradient sequences have the potential to resolve high frequency fluctuations by measuring the turbulent energy spectrum (Dillinger, McGrath, Guenthner, & Kozerke, 2022). Recently, a novel approach was developed to study particle-laden flows where the particles are much smaller than the image resolution. Analogous to light scattering, signal fluctuations at one point in k-space are related to the motion of particles. From the correlation in the signal with respect to time, statistical properties of a particle ensemble can be determined (Herold, Kampf, & Jakob, 2019).

Recently, Hogendoorn et al. (2023) presented a combined experimental and numerical study for particle-laden pipe flow for higher Reynolds numbers and dilute to dense suspensions. A schematic of the experimental setup and the MRI system used in this study are shown in Fig. 7(a) and (b), respectively. For the DNS a computationally efficient Immersed Boundary Method (IBM) is used (Breugem, 2012) with a frictional soft-sphere collision model based on Costa, Boersma, Westerweel, and Breugem (2015). Fig. 8 shows the time-averaged data of both approaches for two selected cases. Here the MRI results are represented by the square and round markers, these correspond to the velocity and concentration profile, respectively. The solid curves represent the IMB results, which was performed for the same flow conditions. A snapshot of the flow from the direct numerical simulations is shown above. For the measurements of the particle volume fraction, a reference measurement was performed to account for the temporal drift in magnetic properties analogous to the application of an internal standard (Mehdizad et al., 2021). This comparison demonstrates the accuracy of MR-based measurement methods for dense suspension flows at higher Reynolds numbers.

3.5. Heat transfer experiments

Over the last 50 years there has been a growing interest in understanding how various system parameters - such as particle size, shape and volume fraction - impact the mechanisms of heat transfer in a range of settings, including fixed-beds, fluidized beds, hoppers, dryers and rotary reactors. Due to its non-invasive nature, MRI has enabled the measurement of temperature distributions within complex geometries, providing a valuable tool to improve heat transfer models (Bruschewski et al., 2021; Gunathilaka, Pringle, & O'Dell, 2021; John et al., 2022). Yet, performing MRI heat transfer experiments in granular media requires the use of particles that are not only MRI sensitive but also exhibit a signal change in the temperature range being studied. Several approaches include the used of hollow particles filled with a temperature-sensitive liquid such as ethylene-glycol (Gladden et al., 2010) or specially engineered particles (Skuntz, Seymour, & Anderson, 2021). The choice of the MRI temperature-sensitive contrast, e.g. signal intensity, chemical-shift, relaxation times or diffusivity variations, relies on the type of particle used. Recently, Skuntz et al. (2021) studied the heat transfer dynamics of a fixed-bed during gas flow by employing the temperature-dependent relaxation time T_2 of encapsulated phase change material (PCM) particles. The

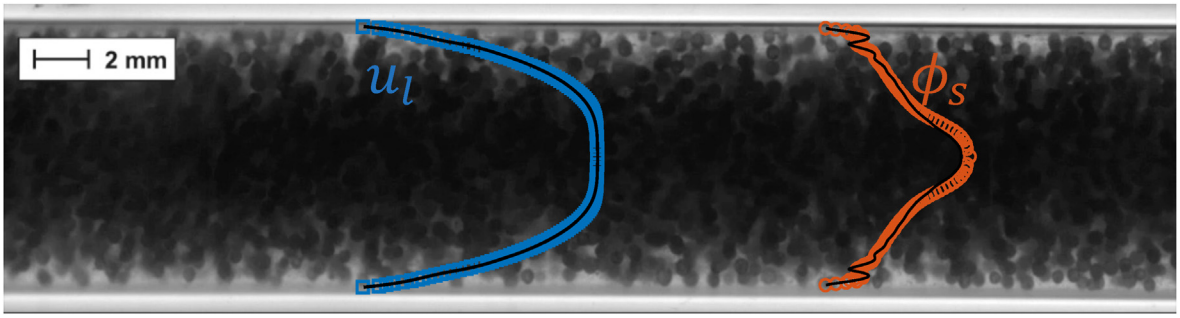

Fig. 6. High-speed camera snapshot of a particle-laden pipe flow. The liquid phase velocity, u_l, and solid volume fraction, φ_s, profiles representing the flow conditions in the pipe mid-plane are superimposed on this image. The markers are results obtained using MRI and the solid lines are results from direct numerical simulations. Figure reproduced from Hogendoorn et al. (2022).

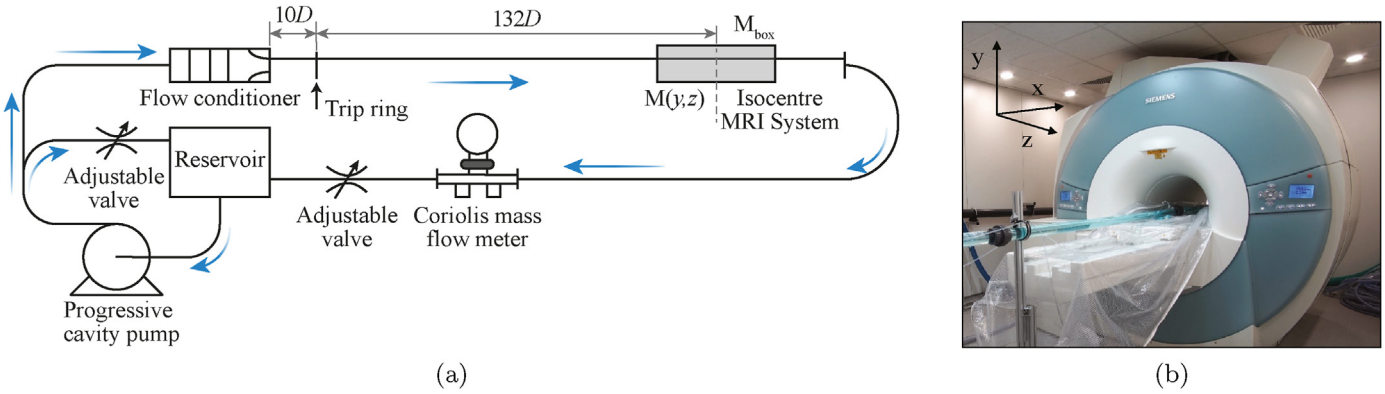

Fig. 7. A schematic overview of the experimental setup (a) and the MRI system (b) used for the study by Hogendoorn et al. (2023).

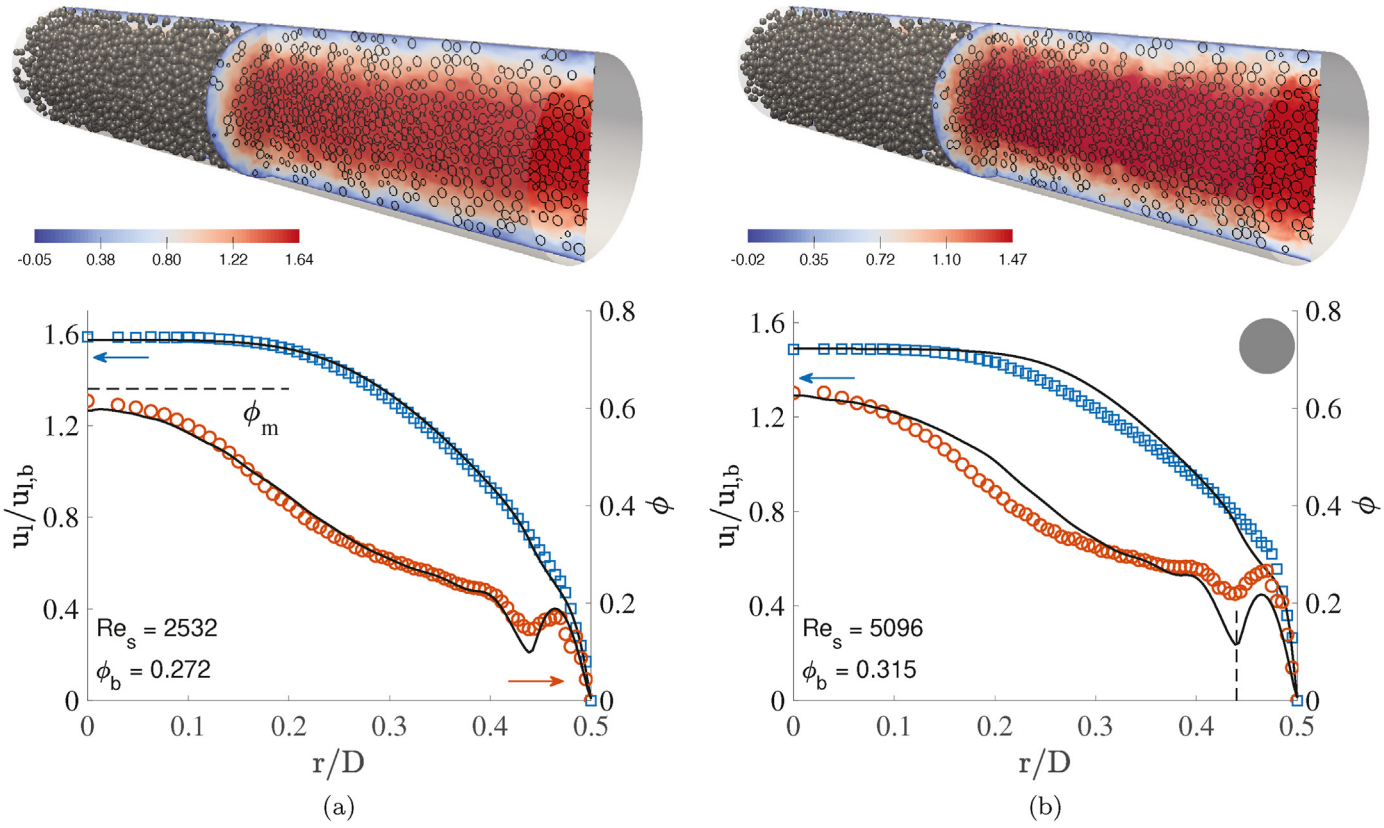

Fig. 8. Top: snapshots of the particle-laden pipe flow from the direct numerical simulations, the color represents the normalized stream-wise velocity; Bottom: the time-averaged velocity and concentration profiles from the MRI (markers) and DNS (solid curves). Adapted from Hogendoorn et al. (2023).

method allowed to successfully monitor temperature gradients within a fixed-bed of PCM particles under C_2F_6 gas flow at 65 °C, shown by Fig. 9(a). Experiments were performed at different gas pressures, changing the gas condition in the bed between gas, supercritical, and near-critical conditions. Temperature gradients can also be measured by monitoring the proton resonance frequency (PRF) shift with temperature, technique which is widely used in the medical field. Recently, Serial et al. (2023) implemented this technique to image the time-dependent temperature gradients in a fixed-bed during heat flow at 60 °C. For this purpose, hollow polypropylene particles filled with a dysprosium-nitrate aqueous solution were used as particles for the fixed-bed. The dynamic temperature measurements facilitated the indirect measurement of the heat transfer coefficient of the bed. A schematic representation of the setup used and obtained temperature field is illustrated in Fig. 9(b).

While MRI has proven to be a suitable technique to measure temperature changes in complex systems, the difficulty in finding suitable MRI sensitive particles and the delicate MRI hardware make it difficult to perform experiments at high-temperatures conditions. As a result, rather moderate temperatures are commonly used, although experiments at high-temperatures or high-pressure have been performed employing specialized equipment (Gladden et al., 2010; Zheng et al., 2023).

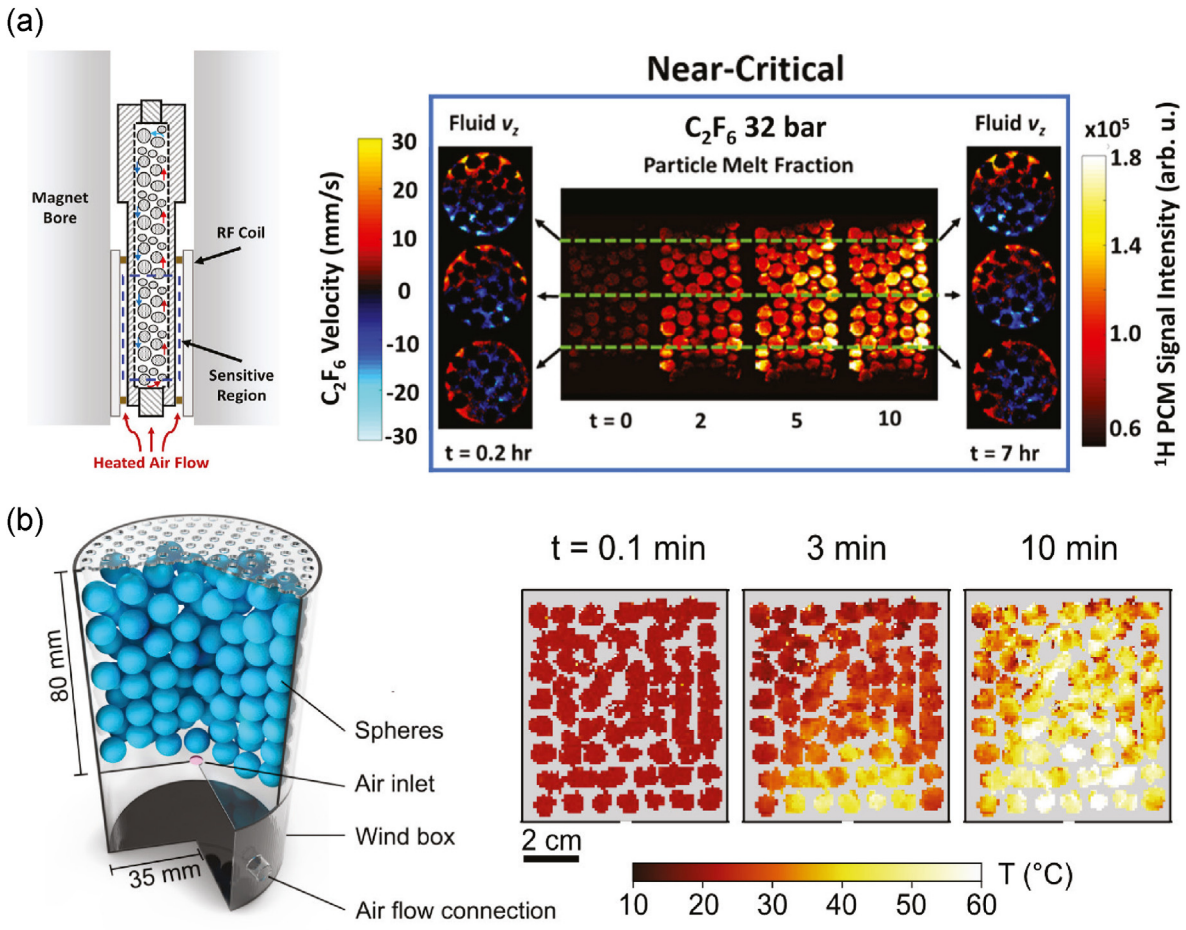

Fig. 9. (a) Schematic of the packed bed system in the magnet bore (25 mm RF coil internal diameter) used and coupled C_2F_6 gas velocity and PCM signal intensity maps at near-critical conditions in Skuntz et al. (2021). (b) Schematic of the packed bed system used by Serial et al. (2023) along with the obtained time-dependent temperature maps.

4. Future developments

4.1. Fast imaging techniques and modern medical MRI methods

Unlike many other tomographic techniques, MRI signal acquisition is sequential, making it an inherently slow process. Over the past decades, a variety of scan acceleration techniques have been developed to increase MRI temporal resolution. These techniques have found extensive use in the field of medical MRI, where reducing scan time improves patient comfort and minimizes examination costs. While some of these acceleration techniques have been partially adopted in the field of engineering, such as compressed sensing (Holland & Gladden, 2014) and parallel imaging (Penn et al., 2017), there is still a broad range of acceleration techniques employed in medical MRI that have not yet found their way into the field of engineering. These techniques include MRI fingerprinting (Ma et al., 2013), image reconstruction by principal component analysis (Zong, d'Eurydice, & Galvosas, 2016), domain transform manifold learning (Zhu, Liu, Cauley, Rosen, & Rosen, 2018), and the combination of compressed sensing and parallel imaging (Otazo, Kim, Axel, & Sodickson, 2010), among others. Such techniques could be successfully applied to study non-stationary dynamic systems with different contrasts, such as multiphase flows and are thus worthwhile to be explored further in the future.

4.2. Contact stress measurement with NMR

Stress imaging is important for understanding the rheological characteristics of granular materials. The state of the art currently involves experimental techniques such as imaging photoelastic disks (Abed Zadeh et al., 2019; Daniels, Kollmer, & Puckett, 2017) and X-ray diffraction of crystalline particles (Hurley, Hall, Andrade, & Wright, 2016). These imaging approaches actually measure strain and the stress is inferred from a constitutive relation for the solid material that the grains are made from. The NMR technique has not been used to measure stress in granular materials because of the difficulty in producing a signal that is sensitive to changes in stress. However, several approaches exist in the literature that offer potential insights into the development for new experiments.

For elastomeric materials, it has been found that the intrinsic transverse relaxation time, T_2, is a suitable proxy variable for strain, where T_2 decays exponentially with increased strain (Nishi & Chikaraishi, 1981). A map of T_2 can be acquired with a suitable pulse sequence (such as spin echo for several echo times). Using the calibration relation, a map of strain is obtained. The stress-strain relation can be used to convert the strain map to produce a stress map (Blümler & Blümich, 1993). The possibility of extending this approach to granular systems has been explored (Elrington, 2018; Frey, 2013). However, these studies were limited by the absence of a strain-relaxation response in the polydimethylsiloxane (PDMS)

samples that were used. This method is likely limited to suitable elastomeric materials that undergo strain-induced crystallisation and may not be feasible for studying systems where granules have a different chemical composition.

The features observed in an NMR spectrum are related to the local electronic environments of the nucleus being studied. Under strain, the interatomic distances change, thus altering the electronic environments experienced by nuclei, resulting in a change in the spectral properties. Zwanziger, Werner-Zwanziger, Shaw, and So (2006) developed a load cell to measure spectra of single crystals under compressive stress. For ^{207}Pb NMR of $Pb(NO_3)_2$, changes in the chemical shift of some of the peaks was observed caused by changes in chemical shielding. For ^{69}Ga NMR of GaP, the linewidth increased due to quadrupolar interaction. Analogous to PRF temperature imaging, stress could be inferred if there is a known calibration relation for stress in terms of the spectral properties.

Fluid pressure was measured with MRI by seeding the flow with lipid-coated microbubbles (Morris, Bencsik, Vangala, & Perrie, 2007, 2008). The microbubbles have a mismatched magnetic susceptibility relative to the surrounding fluid. The susceptibility artefact changes with fluid pressure due to changes in the size of the microbubbles. A suitably viscous suspending fluid is required to minimise microbubble migration caused by buoyancy effects. Microbubbles could be incorporated into liquid capsules to quantify the contact force experienced by particles.

These developments demonstrate the possibility of further expanding the magnetic resonance toolbox to include spatially-resolved strain measurements, thereby inferring the local stress. However, these examples demonstrate that experiments and materials must be designed carefully such that strain responses can be detected and quantified. Stress measurements represent a promising line of inquiry that would enable NMR to measure all major continuum variables relevant to the study of granular materials.

4.3. MRI of pilot scale reactor systems

Scaling up of reactor systems is a crucial task in process engineering. A typical scale-up design process begins at the laboratory scale, where system sizes are in the range of several tens of millimeters. It then progresses to the pilot scale reaching sizes up to approximately 1 m, and eventually to the industrial or production scale, which can be as high as several tens of meters. The flow patterns can change significantly across the scales and hence the results obtained on the lab scale systems are not easily transferable to the production scale. It is important to consider that MRI has certain limitations when imaging larger samples, particularly when compared to other tomographic techniques. As shown in Table 1, MRI systems typically have a limited capacity to accommodate samples beyond a few centimeters in size, unless a clinical scanner is utilized. However, using a clinical scanner may impose restrictions on the experimental setup that can be used. This is particularly relevant for studies of chemical reactors, where a vertical setup is usually preferred for gravity-dominated processes. Additionally, challenges remain in the imaging of samples under high pressure and high temperature conditions.

Fig. 10 illustrates the maximum sample dimensions that can be studied with different MRI systems. Previous MRI works in the field of multiphase and granular flows have predominantly used microimaging systems, enabling imaging samples up to 50 mm in diameter (Müller et al., 2006; Zheng et al., 2023; Harel, Granwehr, Seeley, & Pines, 2006; Kononenko et al., 2022). Although preclinical and clinical MRI platforms can accommodate larger samples, their horizontal orientation is not optimal for many relevant reactor types that typically have a vertical columnar geometry. Hence, one potentially fruitful avenue could be to build MRI

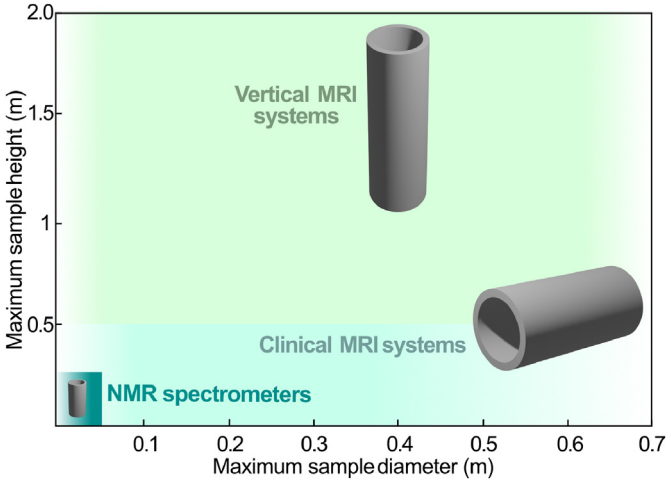

Fig. 10. Diagram illustrating the current and potential MRI platforms for the study of reactor systems. The diagram showcases various MRI setups, including existing systems like NMR spectrometers and clinical MRI systems, as well as a proposed wide bore vertical MRI scanner. It is important to note that the vertical MRI system depicted in the diagram has not been constructed yet and represents a potential future advancement.

systems, that feature a vertically oriented magnet of a bore size similar to clinical MRI magnets. Such an MRI system would allow imaging reactor models of about 300 mm in diameter, and several meters in height, which can be considered pilot scale for many applications. Conducting measurements at such scale would enable to study wall and scale-up effects in a variety of granular and multiphase flow systems, including fluidized beds, spouted beds and spray dryers.

4.4. Low-cost, low-field MRI

MRI remains a niche imaging technique for granular materials because of the limited access to scanners. Scanners are expensive to purchase, require ongoing maintenance, and there is a challenging learning curve to become a proficient operator. The most complex component is the superconducting magnet which requires continuous cryogenic cooling. Recently, the global helium supply chain has been disrupted by world events (Butler, 2017; Anderson, 2018; Bettenhausen, 2022), compromising the operations of hospitals and research laboratories (Siliezar, 2022). Reducing dependence upon liquid helium has led to the development of helium recycling systems (Cryogenic Society of America, 2020), research into high temperature superconducting magnets (Miura et al., 2019; Oya et al., 2018) and the introduction of cryogen-free permanent magnet NMR and MRI systems to the market (Chetcuti et al., 2022; Cooley et al., 2020; Zhen, Dykstra, Gouws, Obruchkov, & Dykstra, 2021). Key advantages of low-field benchtop NMR/MRI scanners compared to a high-field system are that the purchase cost is up to two orders of magnitude lower, maintenance is vastly reduced and the system takes up a much smaller footprint.

The primary disadvantage of low-field MRI is that the detected signal is weaker because spin polarisation and the induced voltage are proportional to the static field (Marques, Simonis, & Webb, 2019). The maximum achievable image resolution is lower because the maximum gradient is about one order of magnitude smaller than what can be attained with a microimaging system. Furthermore, current low-field benchtop systems can only accommodate samples with a diameter below 15 mm, therefore, pilot-scale systems cannot currently be studied. On the other hand,

susceptibility mismatch artefacts are less significant at low fields (Enjilela et al., 2019). Because granular materials usually have strong magnetic susceptibility mismatches between granules and interstitial fluid, low-field devices may serve to improve image quality by minimising artefacts. The increased signal lifetime may facilitate the use of long scan time pulse sequences such as those used in time-resolved imaging.

In addition to these advancements, the recent emergence of open-source MRI scanners and consoles, such as OCRA MRI (OCRA, n.d.), MaRCoS (Negnevitsky et al., 2023), and OSI^2 ONE ("OSI^2 ONE", n.d.), has aimed to mitigate the high cost associated with building and maintaining standard scanners. In the near future, these low-field and open-source setups have the potential to provide increased portability and accessibility, thereby making MRI more accessible for researchers working in the field of granular materials.

4.5. MRI and deep learning

Deep learning has earned significant attention in computer vision applications in recent years, showing successful object recognition, detection and segmentation (Lundervold & Lundervold, 2019). In the context of MRI, deep learning has found applications in two main areas: (i) signal processing, including image reconstruction and restoration, and (ii) image analysis tasks like segmentation, abnormality detection and prediction, particularly in brain, kidney and prostate research.

Deep learning offers a promising solution to speed up and improve MR image reconstruction, which involves a series of customized steps aimed to approximate the appropriate inverse transform to accurately recreate the image. This process becomes particularly challenging when dealing with undersampled data. Moreover, several reconstruction algorithms require prior knowledge of the sample or the measurement of reference images that can account for image imperfections. Recent advancements in neural networks frameworks, such as the automated transform by manifold approximation (AUTOMAP), have shown to significantly improve MRI reconstruction giving comparable results to known reconstruction methods such as model-based iterative reconstruction, sensitivity encoding (SENSE) and compressed sensing MRI reconstruction (Zhu et al., 2018). Therefore, deep learning holds promising implications for the future of MRI reconstruction, regardless of the acquisition protocol used, noise level or undersampling ratio. Furthermore, recent far more advanced methods, such as the introduction of transformers (Vaswani et al., 2017), have further expanded the horizons of deep learning. These new tools offer promising improvements in performance on the aforementioned tasks. For instance, a recent paper utilized a transformer specifically designed for image-based models to enable fast MRI reconstruction (Huang et al., 2022).

In the field of granular MRI, this knowledge could be used to address current challenges such as imperfect imaging reconstruction caused by magnetic susceptibility artefacts, which are commonly encountered in granular media. Deep learning algorithms hold great potential in effectively mitigating these artefacts, thereby enhancing image quality and accuracy. Moreover, the impressive performance of transformers in segmentation tasks offer exciting possibilities for improving segmentation and correlation analysis in highly dynamic systems such as gas-solid fluidized beds. Leveraging the capabilities of transformers can lead to more precise and accurate identification and tracking of gas bubbles or particles, providing valuable insights into the behavior and dynamics of granular systems.

5. Concluding remarks

In summary, we have provided a brief overview of the recent advances of MRI imaging methods for the field of granular and multiphase flows. Developments in MRI hardware and reconstruction techniques have significantly improved the versatility of MRI. This is also evident by the wide application range of MRI, spanning from velocity and concentration measurements in hoppers, fluidized beds, and pipe flows to temperature measurements in packed-beds. Despite these ongoing developments, challenges remain for MR-based measurements in the field of granular media and multiphase flows. These challenges mainly concern the limited frame-rate of MRI and the signal-to-noise ratio. Future developments are mainly foreseen in the field of enhanced image reconstruction algorithms and the availability of low-field MR devices.

Declaration of competing interests

The authors declare that they have no known competing financial interests or personal relationships that could have appeared to influence the work reported in this paper.

Acknowledgements

The authors thankfully acknowledge Prof. dr. ir. C. Poelma (Delft University of Technology) and Prof. D. J. Holland (University of Canterbury) for critical reading of the manuscript and their valuable suggestions. D.C. was supported by the Ministry of Business, Innovation and Employment, New Zealand Endeavour Programme Grant (UOCX1903). The review greatly benefited from the insightful discussions held during the workshop 'Image is Everything', Lorentz Center, Leiden - The Netherlands, 12–16 Sept. 2022.

References

Abed Zadeh, A., Barés, J., Brzinski, T. A., Daniels, K. E., Dijksman, J., Docquier, N., et al. (2019). Enlightening force chains: A review of photoelasticimetry in granular matter. *Granular Matter, 21*(4), 83. https://doi.org/10.1007/s10035-019-0942-2

Altobelli, S. A., Givler, R. C., & Fukushima, E. (1991). Velocity and concentration measurements of suspensions by nuclear magnetic resonance imaging [Publisher: The Society of Rheology]. *Journal of Rheology, 35*(5), 721–734. https://doi.org/10.1122/1.550156

Anderson, S. T. (2018). Economics, helium, and the u.s. federal helium reserve: Summary and outlook. *Natural Resources Research, 27*(4), 455–477. https://doi.org/10.1007/s11053-017-9359-y

Anderson, T. B., & Jackson, R. (1967). Fluid mechanical description of fluidized beds. Equations of motion [publisher: ACS publications]. *Industrial & Engineering Chemistry Fundamentals, 6*(4), 527–539.

Balcom, B. J. (1996). Single-point ramped imaging with t-1 enhancement (SPRITE). *Journal of Magnetic Resonance - Series A, 123*, 131–134.

Bettenhausen, C. (2022). War in Ukraine makes helium shortage more dire. Retrieved March 3, 2023, from *Chemical & Engineering News, 100*(10) https://cen.acs.org/business/specialty-chemicals/War-Ukraine-makes-helium-shortage-more-dire/100/i10.

Binter, C., Knobloch, V., Manka, R., Sigfridsson, A., & Kozerke, S. (2013). Bayesian multipoint velocity encoding for concurrent flow and turbulence mapping [eprint. *Magnetic Resonance in Medicine, 69*(5), 1337–1345. https://doi.org/10.1002/mrm.24370. https://onlinelibrary.wiley.com/doi/pdf/10.1002/mrm.24370

Bruker Biospin. (2020). *Biospec® high field MRI/MRS research (Brochure)*. https://www.bruker.com/en/products-and-solutions/preclinical-imaging/mri/biospec/jcrcontent/root/sections/highlights/sectionpar/highlightfacts/contentpar-4/highlightitem.download-asset.pdf/link/biospec_brochure.pdf.

Blaimer, M., Choli, M., Jakob, P. M., Griswold, M. A., & Breuer, F. A. (2013). Multiband phaseconstrained parallel MRI [eprint. *Magnetic Resonance in Medicine, 69*(4), 974–980. https://doi.org/10.1002/mrm.24685. https://onlinelibrary.wiley.com/doi/pdf/10.1002/mrm.24685

Blümler, P., & Blümich, B. (1993). Investigation of stress distributions in filled polysiloxane by NMR imaging [ISBN: 0323-7648 publisher: Wiley online library]. *Acta Polymerica, 44*(3), 125–131.

Bocquet, L., Losert, W., Schalk, D., Lubensky, T. C., & Gollub, J. P. (2001). Granular shear flow dynamics and forces: Experiment and continuum theory [publisher: APS]. *Physical review E, 65*(1), Article 011307.

Bonn, D., Rodts, S., Groenink, M., Rafai, S., Shahidzadeh-Bonn, N., & Coussot, P. (2008). Some applications of magnetic resonance imaging in fluid mechanics: Complex flows and complex fluids [Publisher: Annual Reviews]. *Annual Review of Fluid Mechanics, 40*, 209–233.

Boyce, C. M., Penn, A., Lehnert, M., Pruessmann, K. P., & Müller, C. R. (2019a). Effect of liquid bridging on bubbles injected into a fluidized bed: A magnetic resonance imaging study. *Powder Technology, 343*, 813–820. https://doi.org/10.1016/j.powtec.2018.11.091

Boyce, C. M., Penn, A., Lehnert, M., Pruessmann, K. P., & Müller, C. R. (2019b). Wake volume of injected bubbles in fluidized beds: A magnetic resonance imaging velocimetry study. *Powder Technology, 357*, 428–435. https://doi.org/10.1016/j.powtec.2019.02.021

Boyce, C. M., Penn, A., Padash, A., Lehnert, M., Pruessmann, K. P., & Müller, C. R. (2019). Anomalous collapse of interacting bubbles in a fluidized bed: A magnetic resonance imaging study [publisher: American physical society]. *Physical Review Fluids, 4*(3), Article 034303. https://doi.org/10.1103/PhysRevFluids.4.034303

Boyce, C. M., Penn, A., Pruessmann, K. P., & Müller, C. R. (2018). Magnetic resonance imaging of gas-solid fluidization with liquid bridging [eprint. *AIChE Journal, 64*(8), 2958–2971. https://doi.org/10.1002/aic.16036. https://onlinelibrary.wiley.com/doi/pdf/10.1002/aic.16036

Boyce, C. M., Rice, N. P., Ozel, A., Davidson, J. F., Sederman, A. J., Gladden, L. F., et al. (2016). Magnetic resonance characterization of coupled gas and particle dynamics in a bubbling fluidized bed [publisher: American physical society]. *Physical Review Fluids, 1*(7), Article 074201. https://doi.org/10.1103/PhysRevFluids.1.074201

Boyce, C. M., Rice, N. P., Sederman, A. J., Dennis, J. S., & Holland, D. J. (2016). 11-interval PFG pulse sequence for improved measurement of fast velocities of fluids with high diffusivity in systems with short t2. *Journal of Magnetic Resonance, 265*, 67–76. https://doi.org/10.1016/j.jmr.2016.01.023

Breuer, F. A., Blaimer, M., Heidemann, R. M., Mueller, M. F., Griswold, M. A., & Jakob, P. M. (2005). Controlled aliasing in parallel imaging results in higher acceleration (CAIPIRINHA) for multi-slice imaging [eprint. *Magnetic Resonance in Medicine, 53*(3), 684–691. https://doi.org/10.1002/mrm.20401. https://onlinelibrary.wiley.com/doi/pdf/10.1002/mrm.20401

Breugem, W.-P. (2012). A second-order accurate immersed boundary method for fully resolved simulations of particle-laden flows. *Journal of Computational Physics, 231*(13), 4469–4498. https://doi.org/10.1016/j.jcp.2012.02.026

Brown, R. W., Cheng, Y.-C. N., Haacke, E. M., Thompson, M. R., & Venkatesan, R. (2014). In *Magnetic resonance imaging: Physical principles and sequence design* (2nd ed.). John Wiley & Sons, Inc.

Brown, R. L., & Richards, J. C. (1965). Kinematics of the flow of dry powders and bulk solids [Publisher: Springer]. *Rheologica Acta, 4*, 153–165.

Brox, T. (2016). *New methods for studying materials under shear with nuclear magnetic resonance [Doctoral dissertation*. Open Access Te Herenga Waka-Victoria University of Wellington.

Bruker Corporation. (2023). *Micro2.5 -MicWB40*. Retrieved June 14, 2023, from https://www.bruker.com/en/products-and-solutions/mr/nmr/mr-microscopy-diffusion/probes/micro2-5-micwb40.html.

Bruschewski, M., Schmidt, S., John, K., Grundmann, S., & Schmitter, S. (2021). An unbiased method for PRF-shift temperature measurements in convective heat transfer systems with functional parts made of metal. *Magnetic Resonance Imaging, 75*, 124–133. https://doi.org/10.1016/j.mri.2020.10.006

Buchholz, H. S., Brummerloh, D. L., Benders, S., & Penn, A. (2023). *The effect of baffles on the hydrodynamics of a gas-solid fluidized bed studied using real-time magnetic resonance imaging*. June 5. https://doi.org/10.48550/arXiv.2306.02938.

Butler, D. (2017). Qatar blockade hits helium supply [number: 7661 publisher: Nature publishing group], 16-16 *Nature, 547*(7661). https://doi.org/10.1038/547016a.

Callaghan, P. T. (1993). *Principles of nuclear magnetic resonance microscopy [Google-Books-ID: yjrjT W5hygC]*. Clarendon Press.

Callaghan, P. T. (1999). Rheo-NMR: Nuclear magnetic resonance and the rheology of complex fluids [publisher: IOP publishing]. *Reports on Progress in Physics, 62*(4), 599.

Candes, E., Romberg, J., & Tao, T. (2006). Robust uncertainty principles: Exact signal reconstruction from highly incomplete frequency information [conference name: IEEE transactions on information theory]. *IEEE Transactions on Information Theory, 52*(2), 489–509. https://doi.org/10.1109/TIT.2005.862083

Chandrasekera, T. C., Li, Y., Moody, D., Schnellmann, M. A., Dennis, J. S., & Holland, D. J. (2015). Measurement of bubble sizes in fluidised beds using electrical capacitance tomography. *Chemical Engineering Science, 126*, 679–687. https://doi.org/10.1016/j.ces.2015.01.011

Chetcuti, K., Chilingulo, C., Goyal, M. S., Vidal, L., O'Brien, N. F., Postels, D. G., et al. (2022). Implementation of a low-field portable MRI scanner in a resourceconstrained environment: Our experience in Malawi [publisher: Am soc neuroradiology]. *American Journal of Neuroradiology, 43*(5), 670–674.

Clarke, D. A., Fabich, H. T., Brox, T. I., Galvosas, P., & Holland, D. J. (2019). On the influence of rotational motion on MRI velocimetry of granular flows-theoretical predictions and comparison to experimental data. *Journal of Magnetic Resonance, 307*, Article 106569.

Cooley, C. Z., Stockmann, J. P., Witzel, T., LaPierre, C., Mareyam, A., Jia, F., et al. (2020). Design and implementation of a low-cost, tabletop MRI scanner for education and research prototyping. *Journal of Magnetic Resonance, 310*, Article 106625. https://doi.org/10.1016/j.jmr.2019.106625

Costa, P., Boersma, B. J., Westerweel, J., & Breugem, W.-P. (2015). Collision model for fully resolved simulations of flows laden with finite-size particles. *Physical Review E, 92*(5), Article 053012. https://doi.org/10.1103/PhysRevE.92.053012

Coussot, P. (2020). Progress in rheology and hydrodynamics allowed by NMR or MRI techniques. *Experiments in Fluids, 61*(9), 207. https://doi.org/10.1007/s00348-020-03037-y

Cryogenic Society of America. (2020). *AFCryo, cryomech collaborate to provide helium recovery, LN2 generation [CSA archive]*. July 6. Retrieved March 3, 2023, from https://cryogenicsocietyarchive.org/2020/07/06/afcryo_cryomech_collaborate_to_provide_helium_recovery_ln2_generation/.

Danczyk, M., Meaclem, T., Mehdizad, M., Clarke, D., Galvosas, P., Fullard, L., et al. (2020). Influence of contact parameters on discrete element method (DEM) simulations of flow from a hopper: Comparison with magnetic resonance imaging (MRI) measurements. *Powder Technology, 372*, 671–684.

Daniels, K. E., Kollmer, J. E., & Puckett, J. G. (2017). Photoelastic force measurements in granular materials [publisher: American institute of physics]. *Review of Scientific Instruments, 88*(5), Article 051808. https://doi.org/10.1063/1.4983049

de Cagny, H., Fall, A., Denn, M. M., & Bonn, D. (2015). Local rheology of suspensions and dry granular materials. *Journal of Rheology, 59*(4), 957–969. https://doi.org/10.1122/1.4919970

Dillinger, H., McGrath, C., Guenthner, C., & Kozerke, S. (2022). Fundamentals of turbulent flow spectrum imaging. *Magnetic Resonance in Medicine, 87*(3), 1231–1249. https://doi.org/10.1002/mrm.29001

Dirix, P., Buoso, S., Peper, E. S., & Kozerke, S. (2022). Synthesis of patient-specific multipoint 4d flow MRI data of turbulent aortic flow downstream of stenotic valves [number: 1 publisher: Nature publishing group]. *Scientific Reports, 12*(1), Article 16004. https://doi.org/10.1038/s41598-022-20121-x

Dyverfeldt, P., Sigfridsson, A., Kvitting, J.-P. E., & Ebbers, T. (2006). Quantification of intravoxel velocity standard deviation and turbulence intensity by generalizing phase-contrast MRI [eprint. *Magnetic Resonance in Medicine, 56*(4), 850–858. https://doi.org/10.1002/mrm.21022. https://onlinelibrary.wiley.com/doi/pdf/10.1002/mrm.21022

Elkins, C. J., & Alley, M. T. (2007). Magnetic resonance velocimetry: Applications of magnetic resonance imaging in the measurement of fluid motion. *Experiments in Fluids, 43*(6), 823–858. https://doi.org/10.1007/s00348-007-0383-2

Elrington, S. A. (2018). *Developing new approaches to faster, high-spatial resolution phosphorus-31 MR imaging of bone [Doctoral dissertation*. Yale University.

Emid, S., & Creyghton, J. (1985). High resolution NMR imaging in solids [Publisher: Elsevier]. *Physica B+C, 128*(1), 81–83.

Enjilela, R., MacMillan, B., McAloon, M. J., Petrov, O. V., Vashaee, S., & Balcom, B. J. (2019). Controlling susceptibility mismatch effects, signal lifetimes, and SNR through variation of b0 in MRI of rock core plugs. *Journal of Magnetic Resonance, 307*, Article 106575. https://doi.org/10.1016/j.jmr.2019.106575

Fabich, H. T., Brox, T. I., Clarke, D., Seymour, J. D., Codd, S. L., Galvosas, P., et al. (2018). Measurements of the velocity distribution for granular flow in a Couette cell. *Physical Review E, 98*(6), Article 062901.

Fabich, H. T., Sederman, A. J., & Holland, D. J. (2016). Development of ultrafast UTE imaging for granular systems. *Journal of Magnetic Resonance, 273*, 113–123. https://doi.org/10.1016/j.jmr.2016.10.016

Fabich, H. T., Sederman, A. J., & Holland, D. J. (2017). Study of bubble dynamics in gas-solid fluidized beds using ultrashort echo time (UTE) magnetic resonance imaging (MRI). *Chemical Engineering Science, 172*, 476–486. https://doi.org/10.1016/j.ces.2017.07.003

Frey, M. A. (2013). *Using novel pulse sequences for magnetic resonance imaging of 31 phosphorus in hard and soft solids [Doctoral dissertation*. Yale University.

Fukushima, E. (1999). NUCLEAR MAGNETIC RESONANCE AS a TOOL TO STUDY FLOW. *Annual Review of Fluid Mechanics, 31*(1), 95–123. https://doi.org/10.1146/annurev.fluid.31.1.95

Fullard, L., Holland, D. J., Galvosas, P., Davies, C., Lagrée, P.-Y., & Popinet, S. (2019). Quantifying silo flow using MRI velocimetry for testing granular flow models. *Physical Review Fluids, 4*(7), Article 074302.

Gentzler, M., & Tardos, G. I. (2009). Measurement of velocity and density profiles in discharging conical hoppers by NMR imaging [Publisher: Elsevier]. *Chemical Engineering Science, 64*(22), 4463–4469.

Gladden, L. F., Abegao, F. J., Dunckley, C. P., Holland, D. J., Sankey, M. H., & Sederman, A. J. (2010). Mri: Operando measurements of temperature, hydrodynamics and local reaction rate in a heterogeneous catalytic reactor [Publisher: Elsevier]. *Catalysis Today, 155*(3), 157–163.

Gladden, L. F., & Sederman, A. J. (2013). Recent advances in flow MRI. *Journal of Magnetic Resonance, 229*, 2–11. https://doi.org/10.1016/j.jmr.2012.11.022

Griswold, M. A., Jakob, P. M., Heidemann, R. M., Nittka, M., Jellus, V., Wang, J., et al. (2002). Generalized autocalibrating partially parallel acquisitions (GRAPPA) [eprint. *Magnetic Resonance in Medicine, 47*(6), 1202–1210. https://doi.org/10.1002/mrm.10171. https://onlinelibrary.wiley.com/doi/pdf/10.1002/mrm.10171

Gunathilaka, I. E., Pringle, J. M., & O'Dell, L. A. (2021). Operando magnetic resonance imaging for mapping of temperature and redox species in thermo-electrochemical cells [number: 1 publisher: Nature publishing group]. *Nature Communications, 12*(1), 6438. https://doi.org/10.1038/s41467-021-26813-8

Hampton, R. E., Mammoli, A. A., Graham, A. L., Tetlow, N., & Altobelli, S. A. (1997). Migration of particles undergoing pressure-driven flow in a circular conduit [Publisher: The Society of Rheology]. *Journal of Rheology, 41*(3), 621–640. https://doi.org/10.1122/1.550863

Han, M., Kim, C., Kim, M., & Lee, S. (1999). Particle migration in tube flow of suspensions. *Journal of Rheology, 43*(5), 1157–1174. https://doi.org/10.1122/1.551019

Harel, E., Granwehr, J., Seeley, J. A., & Pines, A. (2006). Multiphase imaging of gas flow in a nanoporous material using remote-detection NMR [number: 4 publisher: Nature publishing group]. *Nature Materials, 5*(4), 321–327. https://doi.org/10.1038/nmat1598

Herold, V., Kampf, T., & Jakob, P. M. (2019). Dynamic magnetic resonance scattering. *Communications Physics, 2*(1), 46. https://doi.org/10.1038/s42005-019-0136-6

Hindman, J. C. (1966). Proton resonance shift of water in the gas and liquid states [publisher: American institute of physics]. *The Journal of Chemical Physics, 44*(12), 4582–4592. https://doi.org/10.1063/1.1726676

Hogendoorn, W., Breugem, W.-P., Frank, D., Bruschewski, M., Grundmann, S., & Poelma, C. (2023). *From nearly homogeneous to core-peaking suspensions: Insight in suspension pipe flows using MRI and DNS*. August 23. Retrieved August 24, 2023, from http://arxiv.org/abs/2308.12100.

Hogendoorn, W., Bruschewski, M., Frank, D., Breugem, W.-P., Grundmann, S., & Poelma, C. (2022). *Experimental investigation of shear-induced migration in particle-laden pipe flow using MRI [12th International Symposium on Turbulence and Shear Flow Phenomena (TSFP12)*. July 19.

Holland, D. J., & Gladden, L. F. (2014). Less is more: How compressed sensing is transforming metrology in chemistry [eprint. *Angewandte Chemie International Edition, 53*(49), 13330–13340. https://doi.org/10.1002/anie.201400535. https://onlinelibrary.wiley.com/doi/pdf/10.1002/anie.201400535

Holland, D. J., Müller, C. R., Dennis, J. S., Gladden, L. F., & Davidson, J. F. (2010). Magnetic resonance studies of fluidization regimes [publisher: American chemical society]. *Industrial & Engineering Chemistry Research, 49*(12), 5891–5899. https://doi.org/10.1021/ie901450q

Holland, D. J., Müller, C. R., Dennis, J. S., Gladden, L. F., & Sederman, A. J. (2008). Spatially resolved measurement of anisotropic granular temperature in gas-fluidized beds. *Powder Technology, 182*(2), 171–181. https://doi.org/10.1016/j.powtec.2007.06.030

Huang, J., Fang, Y., Wu, Y., Wu, H., Gao, Z., Li, Y., et al. (2022). Swin transformer for fast MRI. *Neurocomputing, 493*, 281–304. https://doi.org/10.1016/j.neucom.2022.04.051

Hurley, R. C., Hall, S. A., Andrade, J. E., & Wright, J. (2016). Quantifying interparticle forces and heterogeneity in 3d granular materials [publisher: APS]. *Physical Review Letters, 117*(9), Article 098005.

Hyperfine Inc. (2023). *Meet swoop® portable MR imaging system™ (Brochure)*. https://hyperfine.io/resources/literature#brochures.

John, K., Wüstenhagen, C., Schmidt, S., Schmitter, S., Bruschewski, M., & Grundmann, S. (2022). Reynolds stress tensor and velocity measurements in technical flows by means of magnetic resonance velocimetry: Data acquisition in the flow field behind the sudden expansion of the FDA benchmark nozzle and identification of systematic errors [Publisher: Oldenbourg Wissenschaftsverlag]. *Tm - Technisches Messen, 89*(3), 201–209. https://doi.org/10.1515/teme-2021-0123

Jop, P., Forterre, Y., & Pouliquen, O. (2006). A constitutive law for dense granular flows [Publisher: Nature Publishing Group UK London]. *Nature, 441*(7094), 727–730.

Jung, J., Gidaspow, D., & Gamwo, I. K. (2005). Measurement of two kinds of granular temperatures, stresses, and dispersion in bubbling beds [publisher: ACS publications]. *Industrial & Engineering Chemistry Research, 44*(5), 1329–1341.

Kawaguchi, T. (2010). MRI measurement of granular flows and fluid-particle flows. *Advanced Powder Technology, 21*(3), 235–241. https://doi.org/10.1016/j.apt.2010.03.014

Köhl, M. H., Lu, G., Third, J. R., Häberlin, M., Kasper, L., Prüssmann, K. P., et al. (2013). Magnetic resonance imaging (MRI) study of jet formation in packed beds. *Chemical Engineering Science, 97*, 406–412. https://doi.org/10.1016/j.ces.2013.04.046

Kononenko, E. S., Svyatova, A. I., Skovpin, I. V., Kovtunova, L. M., Gerasimov, E. Y., & Koptyug, I. V. (2022). Getting the most out of parahydrogen-induced signal enhancement for MRI of reacting heterogeneous systems [publisher: American chemical society]. *Journal of Physical Chemistry C, 126*(35), 14914–14921. https://doi.org/10.1021/acs.jpcc.2c05218

Koval, G., Roux, J.-N., Corfdir, A., & Chevoir, F. (2009). Annular shear of cohesionless granular materials: From the inertial to quasistatic regime [publisher: APS]. *Physical Review E, 79*(2), Article 021306.

Kozak, B. M., Jaimes, C., Kirsch, J., & Gee, M. S. (2020). MRI techniques to decrease imaging times in children [Publisher: Radiological Society of North America]. *RadioGraphics, 40*(2), 485–502. https://doi.org/10.1148/rg.2020190112

Kunii, D., & Levenspiel, O. (1991). *Fluidization engineering [Google-Books-ID: ZVnb17qRz8QC]*. October 25. Butterworth-Heinemann.

Leskovec, M., Lundell, F., & Innings, F. (2020). Pipe flow with large particles and their impact on the transition to turbulence. *Physical Review Fluids, 5*(11), Article 112301. https://doi.org/10.1103/PhysRevFluids.5.112301

Lundervold, A. S., & Lundervold, A. (2019). An overview of deep learning in medical imaging focusing on MRI. *Zeitschrift für Medizinische Physik, 29*(2), 102–127. https://doi.org/10.1016/j.zemedi.2018.11.002

Lustig, M., Donoho, D., & Pauly, J. M. (2007). Sparse MRI: The application of compressed sensing for rapid MR imaging [eprint. *Magnetic Resonance in Medicine, 58*(6), 1182–1195. https://doi.org/10.1002/mrm.21391. https://onlinelibrary.wiley.com/doi/pdf/10.1002/mrm.21391

MacKenzie, J., Söderberg, D., Swerin, A., & Lundell, F. (2017). Turbulent stress measurements with phase-contrast magnetic resonance through tilted slices. *Experiments in Fluids, 58*(5), 51. https://doi.org/10.1007/s00348-017-2328-8

Ma, D., Gulani, V., Seiberlich, N., Liu, K., Sunshine, J. L., Duerk, J. L., et al. (2013). Magnetic resonance fingerprinting [number: 7440 publisher: Nature publishing group]. *Nature, 495*(7440), 187–192. https://doi.org/10.1038/nature11971

Majors, P. D., Givler, R., & Fukushima, E. (1989). Velocity and concentration measurements in multiphase flows by NMR. *Journal of Magnetic Resonance (1969), 85*(2), 235–243. https://doi.org/10.1016/0022-2364(89)90139-X

Marques, J. P., Simonis, F. F., & Webb, A. G. (2019). Low-field MRI: An MR physics perspective [eprint. *Journal of Magnetic Resonance Imaging, 49*(6), 1528–1542. https://doi.org/10.1002/jmri.26637. https://onlinelibrary.wiley.com/doi/pdf/10.1002/jmri.26637

Mehdizad, M. (2021). *Measurement of solid fraction and velocity during granular flow discharge from a silo*. Retrieved March 20, 2023, from. [Doctoral dissertation, University of Canterbury https://scholar.google.com/citations?viewop=viewcitation&hl=en&user=2LbihCYAAAAJ&citationforview=2LbihCYAAAAJ:Tyk-4Ss8FVUC.

Mehdizad, M., Fullard, L., Galvosas, P., & Holland, D. (2021). Quantitative measurements of flow dynamics in 3d hoppers using MRI [Publisher: Elsevier]. *Powder Technology, 392*, 69–80.

Milc, K. W., Serial, M. R., Philippi, J., Dijksman, J. A., van Duynhoven, J. P. M., & Terenzi, C. (2022). Validation of temperature-controlled rheo-MRI measurements in a submillimeter-gap Couette geometry [eprint. *Magnetic Resonance in Chemistry, 60*(7), 606–614. https://doi.org/10.1002/mrc.5157. https://onlinelibrary.wiley.com/doi/pdf/10.1002/mrc.5157

Miura, H., Matsuda, T., Nomura, K., Yokoyama, S., Morita, Y., Otake, S., et al. (2019). Magnetic design of a half-size 5 t high-temperature superconducting coil for MRI [conference name: IEEE transactions on applied superconductivity]. *IEEE Transactions on Applied Superconductivity, 29*(5), 1–5. https://doi.org/10.1109/TASC.2019.2910124

Morris, R. H., Bencsik, M., Nestle, N., Galvosas, P., Fairhurst, D., Vangala, A., et al. (2008). Robust spatially resolved pressure measurements using MRI with novel buoyant advection-free preparations of stable microbubbles in polysaccharide gels. *Journal of Magnetic Resonance, 193*(2), 159–167. https://doi.org/10.1016/j.jmr.2008.04.025

Morris, R. H., Bencsik, M., Vangala, A. K., & Perrie, Y. (2007). Three-dimensional fluid pressure mapping in porous media using magnetic resonance imaging with gas-filled liposomes. *Magnetic Resonance Imaging, 25*(4), 509–512. https://doi.org/10.1016/j.mri.2006.11.021

Moser, K. W., Kutter, E. C., Georgiadis, J. G., Buckius, R. O., Morris, H. D., & Torczynski, J. R. (2000). Velocity measurements of flow through a step stenosis using magnetic resonance imaging [Publisher: Springer]. *Experiments in Fluids, 29*(5), 438–447.

MR Solutions Group Ltd. (2020). *MRS*DRYMAG (Brochure)*. https://www.mrsolutions.com/mrimaging/mr-imaging/mr-dry-magnet-cryogen-free/.

Mudde, R. F. (2010). Double x-ray tomography of a bubbling fluidized bed. *Industrial & Engineering Chemistry Research, 49*(11), 5061–5065. https://doi.org/10.1021/ie901537z

Mueth, D. M., Debregeas, G. F., Karczmar, G. S., Eng, P. J., Nagel, S. R., & Jaeger, H. M. (2000). Signatures of granular microstructure in dense shear flows [number: 6794 publisher: Nature publishing group]. *Nature, 406*(6794), 385–389. https://doi.org/10.1038/35019032

Müller, S. (1988). Multifrequency selective rf pulses for multislice MR imaging [eprint. *Magnetic Resonance in Medicine, 6*(3), 364–371. https://doi.org/10.1002/mrm.1910060315. https://onlinelibrary.wiley.com/doi//pdf/10.1002/mrm.1910060315

Müller, C. R., Davidson, J. F., Dennis, J. S., Fennell, P. S., Gladden, L. F., Hayhurst, A. N., et al. (2006). Real-time measurement of bubbling phenomena in a three-dimensional gas-fluidized bed using ultrafast magnetic resonance imaging. *Physical Review Letters, 96*(15), Article 154504. https://doi.org/10.1103/PhysRevLett.96.154504

Müller, C. R., Holland, D. J., Sederman, A. J., Scott, S. A., Dennis, J. S., & Gladden, L. F. (2008). Granular temperature: Comparison of magnetic resonance measurements with discrete element model simulations. *Powder Technology, 184*(2), 241–253. https://doi.org/10.1016/j.powtec.2007.11.046

Negnevitsky, V., Vives-Gilabert, Y., Algarín, J. M., Craven-Brightman, L., Pellicer-Guridi, R., O'Reilly, T., et al. (2023). MaRCoS, an open-source electronic control system for low-field MRI. *Journal of Magnetic Resonance, 350*, Article 107424. https://doi.org/10.1016/j.jmr.2023.107424OSI2ONE. https://gitlab.com/osii-one (n.d.).

Nishi, T., & Chikaraishi, T. (1981). Pulsed NMR studies of elastomers under large deformation [Publisher: Taylor & Francis]. *Journal of Macromolecular Science, Part B: Physics, 19*(3), 445–457.

OCRA. (n.d.). https://openmri.github.io/ocra/.

Otazo, R., Kim, D., Axel, L., & Sodickson, D. K. (2010). Combination of compressed sensing and parallel imaging for highly accelerated first-pass cardiac perfusion MRI [eprint. *Magnetic Resonance in Medicine, 64*(3), 767–776. https://doi.org/10.1002/mrm.22463. https://onlinelibrary.wiley.com/doi/pdf//10.1002/mrm.22463

Ovarlez, G., Rodts, S., Ragouilliaux, A., Coussot, P., Goyon, J., & Colin, A. (2008). Wide-gap Couette flows of dense emulsions: Local concentration measurements, and comparison between macroscopic and local constitutive law measurements through magnetic resonance imaging [publisher: American physical society]. *Physical Review E, 78*(3), Article 036307. https://doi.org/10.1103/PhysRevE.78.036307

Oya, M., Matsuda, T., Inoue, T., Morita, T., Eguchi, R., Otake, S., et al. (2018). Design and manufacture of half-size 3-t high-temperature superconducting magnet for MRI [conference name: IEEE transactions on applied superconductivity]. *IEEE Transactions on Applied Superconductivity, 28*(3), 1–5. https://doi.org/10.1109/TASC.2018.2792460

Penn, A., Boyce, C. M., Conzelmann, N., Bezinge, G., Pruessmann, K. P., & Müller, C. R. (2019). Real-time magnetic resonance imaging of fluidized beds with internals. *Chemical Engineering Science, 198*, 117–123. https://doi.org/10.1016/j.ces.2018.12.041

Penn, A., Boyce, C. M., Kovar, T., Tsuji, T., Pruessmann, K. P., & Müller, C. R. (2018). Realtime magnetic resonance imaging of bubble behavior and particle velocity in fluidized beds [publisher: American chemical society]. *Industrial & Engineering Chemistry Research, 57*(29), 9674–9682. https://doi.org/10.1021/acs.iecr.8b00932

Penn, A., Boyce, C. M., Pruessmann, K. P., & Müller, C. R. (2020). Regimes of jetting and bubbling in a fluidized bed studied using real-time magnetic resonance imaging. *Chemical Engineering Journal, 383*, Article 123185. https://doi.org/10.1016/j.cej.2019.123185

Penn, A., Tsuji, T., Brunner, D. O., Boyce, C. M., Pruessmann, K. P., & Müller, C. R. (2017). Real-time probing of granular dynamics with magnetic resonance. *Science Advances, 3*(9), Article e1701879.

Pruessmann, K. P., Weiger, M., Scheidegger, M. B., & Boesiger, P. (1999). SENSE: Sensitivity encoding for fast MRI [eprint: *Magnetic Resonance in Medicine, 42*(5), 952–962. https://doi.org/10.1002/(SICI)1522-2594(199911)42:5<952::AID-MRM16>3.0.CO;2-S https://onlinelibrary.wiley.com/doi/pdf/10.1002/28SICI/291522-2594/28199911/2942/3A5/3C952/3A/3AAID-MRM16/3E3.0.CO/3B2-S.

Pure Devices GmbH. (2019). *Lab benchtop MRI training system (Brochure)*. https://www.pure-devices.com/index.php/downloads.html.

Resonint Ltd. (2022). *Ilumr specifications (Brochure)*. https://www.resonint.com/ilumr.

Schmidt, S., John, K., Kim, S. J., Flassbeck, S., Schmitter, S., & Bruschewski, M. (2021). Reynolds stress tensor measurements using magnetic resonance velocimetry: Expansion of the dynamic measurement range and analysis of systematic measurement errors [Publisher: Springer]. *Experiments in Fluids, 62*(6), 121.

Serial, M. R. (2018). *Caracterización hidrodinámica de sistemas multifásicos por RMN* [Doctoral Thesis] [Accepted: 2018-03-13T16:01:38Z]. Retrieved March 21, 2023, from https://rdu.unc.edu.ar/handle/11086/5995.

Serial, M. R., Benders, S., Rotzetter, P., Brummerloh, D. L., Metzger, J. P., Gross, S. P., et al. (2023). *Temperature distribution in a gassolid fixed bed probed by rapid magnetic resonance imaging [Publisher: Elsevier]*. Chemical Engineering Science, Article 118457.

Serial, M. R., Silletta, E. V., Perlo, J., Giovacchini, J. P., Velasco, M. I., Blümich, B., et al. (2019). Single-shot velocity mapping by rewinding of velocity encoding with echo-planar imaging. *Journal of Magnetic Resonance, 307*, Article 106570. https://doi.org/10.1016/j.jmr.2019.106570

Siliezar, J. (2022). *Helium shortage 4.0 makes its way to harvard. Harvard Gazette*. Retrieved March 3, 2023, from https://news.harvard.edu/gazette/story/2022/06/helium-shortage-4-0-makesits-way-to-harvard/.

Skuntz, M. E., Perera, D., Maneval, J. E., Seymour, J. D., & Anderson, R. (2018). Melt-front propagation and velocity profiles in packed beds of phase-change materials measured by magnetic resonance imaging. *Chemical Engineering Science, 190*, 164–172. https://doi.org/10.1016/j.ces.2018.06.019

Skuntz, M. E., Seymour, J. D., & Anderson, R. (2021). Observation of heat transfer due to variable thermophysical properties of sub-, near- and super- critical fluids in porous media by magnetic resonance imaging. *International Communications in Heat and Mass Transfer, 128*, Article 105635. https://doi.org/10.1016/j.icheatmasstransfer.2021.105635

Sodickson, D. K., & Manning, W. J. (1997). Simultaneous acquisition of spatial harmonics (SMASH): Fast imaging with radiofrequency coil arrays [eprint. *Magnetic Resonance in Medicine, 38*(4), 591–603. https://doi.org/10.1002/mrm.1910380414. https://onlinelibrary.wiley.com/doi/pdf/10.1002/mrm.1910380414

Soulat, G., McCarthy, P., & Markl, M. (2020). 4d flow with MRI. *Annual Review of Biomedical Engineering, 22*(1), 103–126. https://doi.org/10.1146/annurev-bioeng-100219-110055

Stannarius, R. (2017). Magnetic resonance imaging of granular materials [publisher: American institute of physics]. *Review of Scientific Instruments, 88*(5), Article 051806. https://doi.org/10.1063/1.4983135

Stevenson, S. J. (2018). *Investigation of shear flow in a planar cylindrical hybrid geometry for rheo- NMR applications [Masters Thesis]*. Victoria University of Wellington [Publisher: Victoria University of Wellington.

Tsuji, T., Penn, A., Hattori, T., Pruessmann, K. P., Müller, C. R., Oshitani, J., et al. (2021). Mechanism of anomalous sinking of an intruder in a granular packing close to incipient fluidization [publisher: American physical society]. *Physical Review Fluids, 6*(6), Article 064305. https://doi.org/10.1103/PhysRevFluids.6.064305

Ulpts, J., Dreher, W., Klink, M., & Thöming, J. (2015). NMR imaging of gas phase hydrogenation in a packed bed flow reactor [Publisher: Elsevier]. *Applied Catalysis A: General, 502*, 340–349.

Vaswani, A., Shazeer, N., Parmar, N., Uszkoreit, J., Jones, L., Gomez, A. N., et al. (2017). Retrieved June 2, 2023, from. *Attention is all you need. Advances in neural information processing systems* (Vol. 30) https://proceedings.neurips.cc/paperfiles/paper/2017/hash/3f5ee243547dee91fbd053c1c4a845aa-Abstract.html.

von Harbou, E., Fabich, H. T., Benning, M., Tayler, A. B., Sederman, A. J., Gladden, L. F., et al. (2015). Quantitative mapping of chemical compositions with MRI using compressed sensing [Publisher: Elsevier]. *Journal of Magnetic Resonance, 261*, 27–37.

Wang, J., Farmani, Z., Dijksman, J. A., Lübeck, C., Speck, O., & Stannarius, R. (2022). Characterization of shear zones in soft granular beds by means of a novel magnetic resonance imaging technique. *Granular Matter, 24*(4), 103. https://doi.org/10.1007/s10035-022-01271-1

Webb, A. G. (2002). January 1). Temperature measurements using nuclear magnetic resonance. In *Annual reports on NMR spectroscopy* (Vol. 45, pp. 1–67). Academic Press. https://doi.org/10.1016/S0066-4103(02)45009-0.

Webb, A. G. (2016). *Magnetic resonance technology: Hardware and system component design*. Royal Society of Chemistry.

Wildman, R. D., Huntley, J. M., Hansen, J.-P., Parker, D. J., & Allen, D. A. (2000). Single-particle motion in three-dimensional vibrofluidized granular beds [publisher: American physical society]. *Physical Review E, 62*(3), 3826–3835. https://doi.org/10.1103/PhysRevE.62.3826

Wlodarczyk, W., Hentschel, M., Wust, P., Noeske, R., Hosten, N., Rinneberg, H., et al. (1999). Comparison of four magnetic resonance methods for mapping small temperature changes. *Physics in Medicine and Biology, 44*(2), 607–624. https://doi.org/10.1088/0031-9155/44/2/022

Zenger, I. (2014). *Magnetic resonance imaging at siemens. Siemens AG*. https://marketing.webassets.siemens-healthineers.com/1800000001924325/4072b7a99020/SiemensMRIMAGNETOMWorldMR-BasicsMRI-brochureenglish1800000001924325.pdf.

Zhen, J., Dykstra, C., Gouws, G., Obruchkov, S., & Dykstra, R. (2021). Mobile low field magnetic resonance hardware development. *Journal of Magnetic Resonance, 322*, Article 106852. https://doi.org/10.1016/j.jmr.2020.106852

Zheng, Q., Williams, J., van Thiel, L. R., Elgersma, S. V., Mantle, M. D., Sederman, A. J., et al. (2023). Operando magnetic resonance imaging of product distributions within the pores of catalyst pellets during fischer-tropsch synthesis [number: 2 publisher: Nature publishing group]. *Nature catalysis, 6*(2), 185–195. https://doi.org/10.1038/s41929-023-00913-8

Zhu, B., Liu, J. Z., Cauley, S. F., Rosen, B. R., & Rosen, M. S. (2018). Image reconstruction by domaintransform manifold learning [number: 7697 publisher: Nature publishing group]. *Nature, 555*(7697), 487–492. https://doi.org/10.1038/nature25988

Zong, F., d'Eurydice, M. N., & Galvosas, P. (2016). Fast reconstruction of highly undersampled MR images using one and two dimensional principal component analysis. *Magnetic Resonance Imaging, 34*(2), 227–238. https://doi.org/10.1016/j.mri.2015.10.009

Zwanziger, J. W., Werner-Zwanziger, U., Shaw, J. L., & So, C. (2006). Stress, strain, and NMR [ISBN: 0926-2040 publisher: Elsevier]. *Solid State Nuclear Magnetic Resonance, 29*(1), 113–118.